CONFIDENTIAL

Precise Data-Driven Modelling of Reticle Heating Induced Spatial Deformations for Correcting Non-Moving Average Effects

Applied to DUV Systems

Navdeep Tripathy

Master of Science Thesis

TU Delft Delft University of Technology

Delft Center for Systems and Control

MSCCONFIDENTIAL

Precise Data-Driven Modelling of Reticle Heating Induced Spatial Deformations for Correcting Non-Moving Average Effects Applied to DUV Systems

Master of Science Thesis

For the degree of Master of Science in Systems and Control at Delft University of Technology

Navdeep Tripathy

November 27, 2018

Faculty of Mechanical, Maritime and Materials Engineering (3mE) · Delft University of Technology

The work in this thesis was supported by ASML. Their cooperation is hereby gratefully acknowledged.

Delft University of Technology
Department of
Delft Center for Systems and Control (dcsc)

The undersigned hereby certify that they have read and recommend to the Faculty of Mechanical, Maritime and Materials Engineering (3mE) for acceptance a thesis entitled

Precise Data-Driven Modelling of Reticle Heating Induced Spatial Deformations for Correcting Non-Moving Average Effects

by

Navdeep Tripathy

in partial fulfillment of the requirements for the degree of

Master of Science Systems and Control

Dated: November 27, 2018

Supervisor(s):

Prof.dr.ir. J.W. van Wingerden

Dr.ir. Kim Batselier

Ir. Nick Kant

Reader(s):

Dr.Ir. Hassan HosseinNia

"Technology, like art, is a soaring exercise of the human imagination"
— *Daniel Bell*

PRECISE DATA-DRIVEN MODELLING OF RETICLE HEATING INDUCED SPATIAL DEFORMATIONS FOR CORRECTING NON-MOVING AVERAGE EFFECTS

Navdeep Tripathy, *Jan-Willem Van Wingerden*, *Kim Batselier*
SYSTEMS AND CONTROL, FACULTY OF MECHANICAL, MARITIME AND MATERIALS ENGINEERING, TU DELFT
and
Nick Kant
FC-64, IMAGE ALIGNMENT, METROLOGY GROUP, ASML

In this paper, the challenge of precisely developing a data-driven Linear Time Invariant MIMO Reticle Heating Induced Deformation Prediction (RHIDP) model for ASML's DUV systems is presented to the reader. The model is developed for two inputs, [redacted]. *A reduced order data-driven based approach for developing a RHIDP model for various* [redacted] *is presented in this paper. This prediction model will be used for precisely estimating the global reticle deformation geometry as well as* [redacted]. *The identified* [redacted] *model exhibits a very high degree of prediction accuracy for a broad working envelope, the prediction is accurate to within a range of* [redacted], *with 99% variances accounted for (VAF) values for all* [redacted]. *This model can thus be used for precise* [redacted].

Categories and Subject Descriptors: I.6.4 [**Simulation and Modelling**]: Model Validation and Analysis; G.1.6 [**Numerical Analysis**]: Optimization; G.1.1 [**Numerical Analysis**]: Interpolation; G.1.8 [**Numerical Analysis**]: Partial Differential Equations

Additional Key Words and Phrases: *System Identification, Black-Box Modelling, Grey Box Model, Linear Time Invariant Model, Machine Learning, Data-driven Identification, Data Mining, Pattern Recognition*

1. INTRODUCTION

Photo-lithography is a process of printing fine nano-meter scale geometric patterns from a photo-mask to a light sensitive photo-resist on a silicon substrate for developing integrated circuits (ICs) . The geometric patterns etched on the substrate are present on the reticle. [redacted] significant factors which affect the overlay precision of DUV lithography systems of ASML. These effects can be corrected using a feed-forward prediction model and a control algorithm. ICs are a part of our everyday life, they form the basis of electronic networks present in all devices used everyday. The ICs are essentially semi-conductors, which contain fine electrical circuits, printed using photo-lithography. Photo-lithography is a micro-fabrication process, performed using state of the art systems having high level precision. [Tripathy 2018]. Precision of the lithography machines is a key factor in helping accurately print ICs, which have features in the scale of nano-meters.

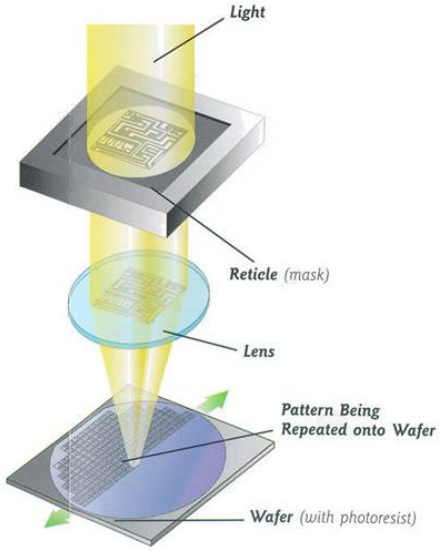

Fig. 1. Wafer exposure illustration, [Willson Research Group, UT Austin]

During Photo-lithography, nano-meter scale geometric patterns present on the reticle, are etched onto the substrate present on the semiconductor (silicon) wafer. During the process, Deep Ultra-Violet (DUV) light is exposed over the reticle, which transfers the pattern on the mask onto the wafer surface containing the substrate.

The work in this thesis was supported by ASML and TU Delft. Their cooperation is hereby gratefully acknowledged.

During the exposure process, DUV light passes through the reticle stage and the projection lens onto the wafer. An illustration of the wafer exposure process is shown in figure 1.

1.1 Reticle Heating

A fraction of the energy from the incident DUV light, is absorbed by the reticle, specifically by the chrome layer, present at the bottom of the reticle. [Tripathy 2018]. Figure 2 illustrates absorption and transmission of the energy from illuminated DUV light through the reticle. Absorption of energy from the DUV light, leads to heating of the reticle. The effect is also termed as Reticle Heating (RH). RH is responsible for two primary effects which affects the precision of ASML's Twinscan lithography systems, namely :

(1) RH induced thermal reticle deformation.
(2) RH induced non-MA effects.

These two effects will be explained in the sub-sections to follow:

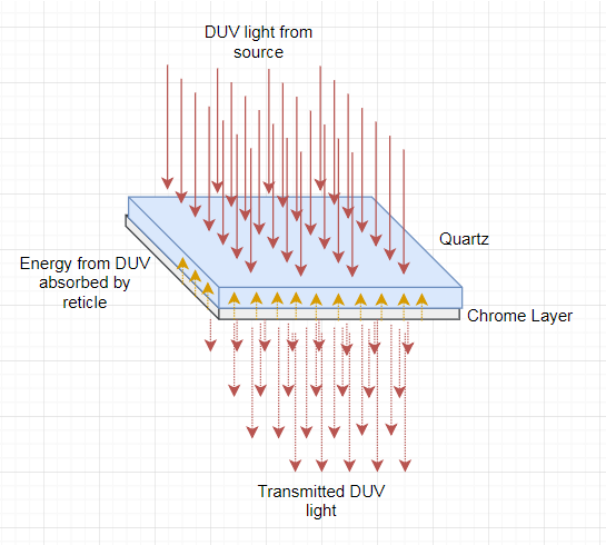

Fig. 2. Energy absorption by Reticle

1.2 RH induced thermal reticle deformation

[redacted]. Deformed mask pattern leads to inaccurate etching on the wafer surface, and is a cause of serious concern for precise imaging preformed by photo-lithography systems. The thermally induced distortions in the geometric pattern can be corrected by precise movement of the lens and reticle stages using a feed-forward prediction model.

In order to correct the effects of thermally induced distortions, the controller which controls the movement of the lens and reticle stage[Tripathy 2018], requires a mathematical prediction model which accurately predicts the global reticle deformation for different DUV light settings (measured in dose J/m^2 / Irradiance $J/s.m^2$). The model is Linear Time Invariant (LTI) in nature as presented in [Kant 2017]. The physical description of the prediction model currently used by ASML is presented in subsection 1.2.1.

Note 1 :

[redacted]

1.2.1 *Current Prediction System.* :

[redacted]. The state and output equations of the current prediction model can be expressed using the following first principle relationship [Kant 2017]:

$$\dot{T}_r(t)_{[m\times 1]} = -\boldsymbol{SG^{-1}}_{[m\times m]} T_r(t)_{[m\times 1]} + \boldsymbol{B}_{m\times 1}[I(t)] \quad (1)$$

$$D(t)_{[32\times 1]} = \boldsymbol{EM^{-1}}_{[32\times m]} T_r(t)_{[m\times 1]} \quad (2)$$

Where,

(1) G : [redacted]
(2) M : [redacted]
(3) S : [redacted]
(4) E : [redacted]
(5) T : [redacted]
(6) D : [redacted]
(7) I : [redacted]
(8) m : [redacted]
(9) B : [redacted]

Please refer to Appendix A for [redacted] *[van der Wielen 2010].*

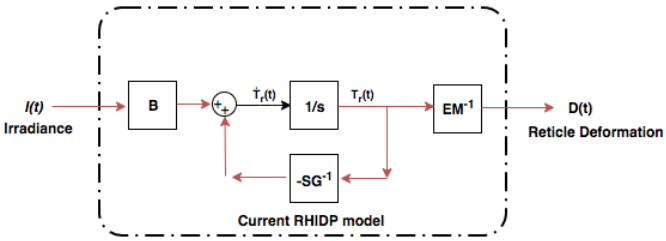

Fig. 3.

1.3

, [Tripathy 2018],

.

(

.

. [Lammers 2016] .

[Lammers 2016].

This in effect necessitates a **new** RHIDP model .

1.3.1 ***New Prediction System.*** :

:

(1)

(2)

.

.

.

The work presented in this paper, sheds light on developing a purely data-driven prediction model, for various Use Cases (UCs). An approach to develop a precise open-loop data-driven RHIDP model for the new reticle deformation behaviour will be the focus of the thesis work presented in this article.

> **Note 2** :
> **What are Use Cases :**
>
> Use Cases (UCs) represent time independent combinations of both inputs within the region of operation, which are kept constant for the entire duration of the experiment. In essence each UC represents a step input for the system.

1.4 Why A Data-Driven Model ?

Data driven modelling techniques provide a useful alternative to Finite Element Method (FEM) based modelling strategies for many industrial applications. In particular at ASML, where there are strict requirements on model accuracy.

The primary reasons for developing a data-driven RHIDP model are :

(1)

(2)

(3)

All the experiments associated with developing the new RHIDP model are based on simulation of a physics based FEM model embedded in the metrology simulator which mimics the DUV systems of ASML.

.

1.5 Problem Statement

Developing an accurate deformation prediction model, .

[redacted]		
1		
2		
3		
4		
5		
6		
7		
8		
9		
10		
11		

Table I.

Metrology Simulator Parameters

[redacted].

The problem statement gives way to the following research questions. These questions will be answered in subsequent sections of this article.

(1) Using physical equations, describe the behaviour of the proposed RHIDP model. Derive and represent the relationship of the inputs with respect to the output in state-space notation.
(2) Owing to the high precision requirements from the new RHIDP model, thoroughly verify the system behaviour using data collected from the metrology simulator [redacted].
(3) [redacted].
(4) Perform a quantification to determine the prediction accuracy of the calibrated model for different static and dynamic inputs.

The block diagram shown in in figure 4 shows the section wise flow of work presented in this article which sequentially answer each of the research questions.

2. NOVEL FIRST PRINCIPLE DESCRIPTION OF A NEW RHIDP MODEL

[redacted].

2.1 Analyzing lumped mass single dimension reticle

The heat absorbed from the DUV light by the chrome layer at the bottom of the reticle, is transmitted vertically to the top, which acts as a heat sink, due to the continuous airflow on the reticle surface. The heat transfer at any given point on the reticle occurs predominantly in the z axis within the reticle, a heat balance

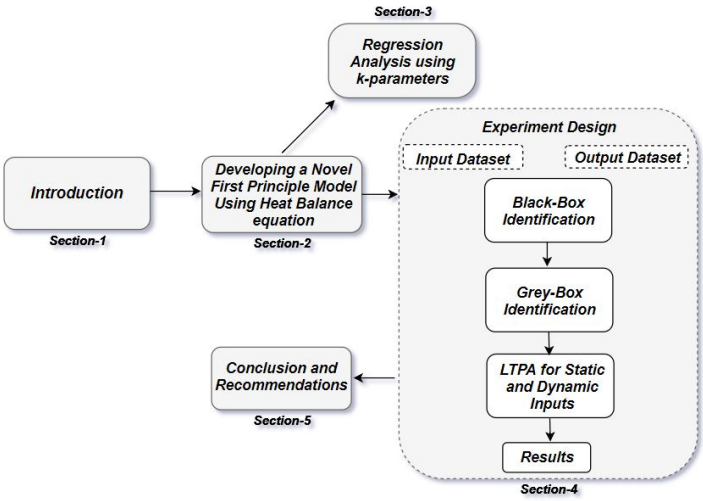

Fig. 4. Block diagram showing the flow of work presented in this report

analysis of a finite element is performed. An analysis of the equations will shed light on the relationship between the inputs and the temperature modes of the reticle, [redacted].

Given a finite reticle volume with a constant thickness z, the heat energy balance relationship is given by the following equation [van der Wielen 2010] :

$$z\frac{\partial}{\partial x}\Big(k_x\frac{\partial T_r(x,y,t)}{\partial x}\Big)+z\frac{\partial}{\partial y}\Big(k_y\frac{\partial T_r(x,y,t)}{\partial y}\Big)+zQ(x,y,t)$$
$$+F(x,y,t)=z\rho c_p\frac{\partial T_r(x,y,t)}{\partial t}+2h(T_r(x,y,t)-T_a(t)) \quad (3)$$

In the equation, the effects of heat loss, due to radiation is neglected, this is due to its 4^{th} order dependence on the absolute temperature of the reticle. A general formulation of the differential equation is provided in the following simplified heat transfer equation:

$$z\nabla.(K.\nabla T_r(t))+zQ+F(t)=z\rho c_p\dot{T}_r(t)+2h(T_r(t)-T_a(t)) \quad (4)$$

Where,

(1) T_r is the reticle temperature. (K)
(2) T_a is the airflow temperature. (K)
(3) Q is the heat generated internally within the reticle. (W/m^3)
(4) F is the externally applied heat load on the reticle surface due to irradiance. (W/m^2)
(5) $z\nabla.(K.\nabla T_r)$ is the gradient of heat flow.
(6) $z\rho c_p\dot{T}_r$ is the energy stored in the finite element.
(7) $2h(T_r-T_a)$ represents the heat lost due to convective cooling with a heat transfer coefficient h.

Note 3 :

$$h = \frac{E}{T_r - T_a} \tag{5}$$

Simplifying equation 4, and collecting terms associated with the reticle temperature T_r, and collecting the sources adding energy to the reticle, the following simplified equation for a finite element is obtained.

$$KT_r(t) + I(t) = \rho c_p \dot{T}_r(t) + 2h(t)(T_r(t) - T_a(t)) \tag{6}$$

$$\dot{T}_r(t) = (\rho c_p)^{-1}(K - 2h(t))T_r(t) + (\rho c_p)^{-1} I(t) + (\rho c_p)^{-1} 2h(t) T_a(t) \tag{7}$$

Note 4

The explanation given in note 2 delineates that the variation in convection coefficient is very minimal, as such the metrology simulator isn't designed to account in the variations in the convection coefficient. Therefore, the conduction and convection matrix presented in equation 7 is considered to to be time invariant, the equation converges to the following relationship:

$$\dot{T}_r(t)_{m\times 1} = -\boldsymbol{G^{-1}} \boldsymbol{S}_{m\times m}.T_r(t)_{m\times 1} + \begin{bmatrix} \boldsymbol{G^{-1}} & \boldsymbol{H} \end{bmatrix}_{m\times 2} \begin{bmatrix} I(t) \\ T_a(t) \end{bmatrix} \tag{8}$$

Where,

(1) S : Conduction and Convection Matrix, includes the effects of conduction (K) and convection ($h(t)$). Considered time-invariant due to minimal variation in convection coefficient with respect to time.
(2) G : Heat capacity matrix, (ρc_p).
(3) T_a : Scaled airflow temperature. (K)
(4) I : Scaled irradiance. (J/m^2)
(5) H : Scaling on T_a. Time varying parameter.
(6) m : number of temperature modes describing the temperature profile for the finite element.

The output equation is given by:

$$D(t)_{[32\times 1]} = \boldsymbol{EM^{-1}_{[32\times m]}}.T_r(t)_{[m\times 1]} \tag{9}$$

Where,

(1) D : Deformation Vector ($meter$).
(2) E : Thermo-mechanical coupling matrix.
(3) M : Mass matrix.

The dynamics of the new RHIDP model shown using equations 8 and 9 indicate LTI nature of the system under certain assumptions.

Note 5

[Michel Verhaegen 2007],

The states identified using measurement data may need not necessarily be associated with the temperature of reticle. This shall be discussed in section 4.3 with more detail. The equations 8 and 9 form a state-space representation of the new RHIDP model with irradiance $I(t)$ and airflow temperature $T_a(t)$ as inputs and deformation vector $D(t)$ as the output. The m^{th} other state-space notation for the new RHIDP model derived using physical equations can be presented in it's equivalent state and output equations :

State Equation :

$$\dot{x}(t)_{[m\times 1]} = \boldsymbol{A_c}_{[m\times m]}.x(t)_{m\times 1} + \boldsymbol{B_c}_{[m\times 2]} u(t)_{[2\times 1]} \tag{10}$$

Output equation:

$$y(t)_{[16\times 1]} = \boldsymbol{C_c}_{[16\times m]}.x(t)_{[m\times 1]} \tag{11}$$

A discretization of the system matrices using **forward euler approximation** with sampling interval chosen as RA instances, generates the following equivalent discrete time state-space representation of the system :

State Equation :

$$x(n+1)_{[m\times 1]} = \boldsymbol{A_d}_{[m\times m]}.x(n)_{[m\times 1]} + \boldsymbol{B_d}_{[m\times 2]}u(n)_{[2\times 1]} \quad (12)$$

Output equation:

$$y(n)_{[16\times 1]} = \boldsymbol{C_d}_{[16\times m]}.x(n)_{[m\times 1]} \quad (13)$$

y, u x represent the output, inputs and states of the system respectively. Where **A**, **B** and **C** are constant and time-independent system matrices. n is used to indicate the time instances for the discretized model. The evolution of state $x(n)$ is linearly related to the inputs $u(n)$ of the system, indicating a Linear Time Invariant description of the RHIDP model.

Note 6
No direct feedthrough :

An import observation from the first principle analysis reveals that there exists no direct feed-through from the inputs on the global reticle deformation magnitude. In other words, the **D** matrix of the system is zero, in continuous and discrete time. This result will play a key role in identifying a data-driven RHIDP model explained in section 4.3.

Please refer to Appendix-C for more information on the combined effects which lead to marginal non-linearity in new RHIDP model.

It should be pointed out that, the state-space representation of the RHIDP system is Linear Time Invariant under the following two assumptions, namely :

(1) Heat lost from the reticle through radiation is neglected in the heat balance equation 3. This is due to 4^{th} order dependence of radiation on the absolute temperature of the reticle and it's surrounding.

(2) The time dependent variation of heat transfer coefficient h on the conduction and convection matrix S is considered to be negligible and the matrices are considered constant in the metrology simulator using which the model is developed.

Both the assumptions hold true on the metrology simulator. In section 3, a step-response analysis of the system on the metrology simulator will be performed in order to understand the MIMO Reticle deformation behaviour. The step-response analysis will also aid in development of the data-driven RHIDP model for static inputs (Use Cases).

3. ANALYSIS OF THE SYSTEM USING THE K FACTOR MODEL FOR STATIC INPUTS

In the previous section, mathematical formulation using the heat balance analysis, converging to a state space description of a m^{th} order prediction model was presented to the reader. An account of the possible reasons responsible for non-linearity in the new deformation prediction model along with assumptions under which, the system can be considered linear was also presented to the reader. Owing to the precision requirements of photo-lithography, in this section, an accurate quantification and validation of the system behaviour, through a step response analysis using measured (k_4/m_y) data on the metrology simulator will be provided. This will also help understand the system behaviour for static inputs (Use cases) around which a precise data-driven prediction model is developed and elaborated to the reader in section 4. However, before proceeding with the analysis, properties of k_4 parameter and why is it used for the analysis will be furnished to the reader.

Note 7
[redacted]:

[redacted]

3.1 Relevance of k_4 parameter

As previously explained in [Tripathy 2018], reticle deformation behaviour is conventionally characterized using k-factors. k-factors are coefficients of basic polynomial shapes, (described using the shape's dependency on x and y axis on the reticle surface). These polynomial shapes are used for decomposing the global reticle deformation on the resist at a given instant, into it's constituent k-factor shapes. In other words, k-factor shapes are used for decomposition of the global reticle deformation shape, into it's constituent local deformation shapes. Their coefficients, represented by k-factors, accommodate the temporal variation in the magnitude of the shapes they represent. In general, the grid distortions in x and y, for a given PARIS [Tripathy 2018] mark at instant $n+1$ on the reticle surface, can be described using the k-factor model given below [Bogers 2011] :

The deformations observed at the [redacted] marks are related to the [redacted] through the following over determined set of equations :

The k-factors are computed using a least squares fit of dx and dy measurement data, at a given time instant, using [redacted] spatially distributed measurement points on the reticle surface along x and y axis by solving equations [redacted]. [redacted] originally developed the k-factor model for characterizing intra-field distortions.

[Bogers 2011].

Please refer to Appendix-D for a graphic representation of all the shapes associated with even and odd k-factors which are used for characterizing global deformations in y and x axis respectively.

One such k-factor of interest is $k_4(n)$, also called magnification in y (m_y). Figure 5, illustrates the shape associated with $k_4(n)$, y^1x^0 is it's associated monomial. $k_4(n)$ represents the magnitude of expansion/contraction purely along y axis. It essentially encapsulates the component of global reticle deformation along the y axis. $k_4(n)$ signal will be used for analyzing the temporal magnitude of reticle deformation for the new RHIDP model. [redacted]. The black horizontal lines shown in figure 5, indicates the height of the associated k_4 shape, following a step-response at UC 291 K, 6.25 J/m^2 at n_3. (304.7 seconds). (Illustrating global contraction of the reticle along y axis). Owing to the absence of magnification effects of the projection lens, $k_4(n)$ presents a very accurate relationship between itself and the actual global deformation of the reticle.

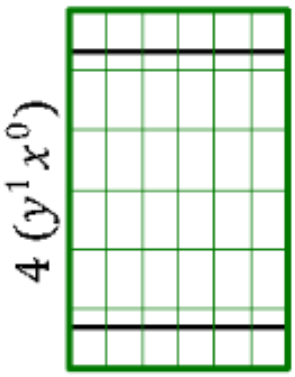

Fig. 5. Shape associated with $k_4(n)$ parameter. The black horizontal lines represent the steady state height of the shape following a step response for a certain UC. y^1x^0 is the monomial associated with k_4

Note 8
Why k_4 ?:

The signal $k_4(n)$ is measured on the metrology simulator. It is one of the two k-factors (other being $k_{18}(n)$), which is uninfluenced by projection lens movements below the reticle. [van den Berg 2018]. As a consequence the magnitude of $k_4(n)$ at any instant, accurately represents the effect of both inputs on the global reticle deformation at instant n for the new RHIDP model.

Note 9:
[redacted]:

[redacted] [Tripathy 2018], [redacted]. [Pen 2016]

[redacted] [Lammers 2016] [redacted]. [Kunnen 2016][Tripathy 2018].

Note 10:
What is a Linear system ?:

A system is said to be linear, if it satisfies the superposition principle, in the sense that the following two properties are satisfied. [Won Y Yang 2009]

—**Additivity** - The response of the system actuated by two or more inputs is the sum of the individual responses of the system to each actuation independently..

—**Homogeneity** - The output of a system to a single independent input is proportional to the input.

As an extension to the property of homogeneity, a linear system satisfies zero input-zero output condition.
These two conditions are necessary and sufficient to validate linearity of a system. Both of the conditions will be substantiated in the sub-sections to follow.

3.2 Numerical analysis to demonstrate the law of Additivity

An experimental analysis using step response data is performed for verifying the linearity of the system. In this sub-section, the property of additivity will be performed, followed by verification of the property of homogeinity in the next sub-section. A system which satisfies the additivity property; when excited by an input $U_1(n)$ generates an output $Y_1(n)$, and for an input $U_2(n)$ generates an output $Y_2(n)$. Then, the system when excited by signal $U_1(n)$ + $U_2(n)$ would generate a response equivalent to $Y_1(n)$ + $Y_2(n)$ as the output. Step response data is collected from the metrology simulator for various UCs, an analysis will be performed to verify the property of additivity for the two input one output linear system, by providing a step signal for u_1 (airflow temperature) and u_2 (dose) individually while keeping the other input at zero. In the new RHIDP model, airflow temperature at 295 K and dose at 0 J/m^2 yields negligible deformation on the reticle. [redacted]. Step response k_4

data collected for UC_1, with u_1 = 295 K and u_2 = $0 J/m^2$, is shown in [redacted]. (Please note the scaling by a factor of 10^{-4} J/m^2 in k_4 plot). Thus, UC_1 295 K and 0 J/m^2 will be considered as a 'virtual' zero input for identifying the new RHIDP model. However, as can be deduced from [redacted], the system exhibits certain **minimal** dynamics (in the scale of 10^{-4}) in k_4 for the 'virtual' zero inputs, and doesn't satisfy the zero input-zero output condition. Thus indicating that, the system is not perfectly linear. As generally expected from real world systems.

In the first experiment, a step input $U_1(n)$ (UC_2) is given, with $u_2(n)$ = 6.25 J/m^2, $u_1(n)$ = 295 K (virtual zero for $u_1(n)$), the dynamics $Y_1(n)$ obtained using $k_4(n)$ is shown in [redacted].

Note 11
Why step response analysis ?:

Step response analysis of a dynamical system with a given initial state condition reveals how the system responds to a sudden input. Equation 3 indicated that reticle heating/cooling is a first order behaviour, as such a first order signal is sufficient to excite the dominant temperature mode of the system.

In particular, important parameters such as rise time, settling time and time-constant of a linear dynamic stable system can be obtained. Unlike impulse response, a step response helps obtain the DC gain of the system. A step response is a simple yet effective way to analyze two important effects, namely transient and a steady state response of the dynamical system. It is one of the most widely used signals by engineers and researchers alike for validating linear system behaviour through experiments. A regression analysis using step response data collected from the system will help shed light on the relationship between the inputs u_1,u_2 and output k_4 for the new RHIDP model to be identified.

Similarly, for the second experiment, a step input $U_2(n)$ (UC_3) is given, with $u_1(n)$ = 291 K, $u_2(n)$ = 0 J/m^2 (virtual zero), the dynamics $Y_1(n)$ obtained using $k_4(n)$ is shown in [redacted]. In the last experiment, a step input $(U_1(n) + U_2(n))$, (UC_4) is provided to the system, with $u_1(n)$ = 291 K, $u_2(n)$ = 6.25 J/m^2. The generated k_4 dynamics is shown in [redacted]. UC_4 is selected in order to validate the property of additivity for the RHIDP model. To this end, during the experiment, three time instances (n_1, n_2, n_3) are considered, n_1, n_2 are instances for the transient response of the system, while n_3 shows a value closer to the steady state response. n_1 represents the 13^{th} RA instant (n = 13), n_2 represents the 26^{th} RA instant (n = 26) and n_3 represents the 40^{th} RA instant (n = 40). This data is tabulated in table II.

Table : 2 [redacted]			
u_1 (K), u_2 (J/m^2)	100 s (n_1)	200 s (n_2)	304.7s (n_3)
$UC_1(295, 0)$	[redacted]	[redacted]	[redacted]
$UC_2(295, 6.25)$	[redacted]	[redacted]	[redacted]
$UC_3(291, 0)$	[redacted]	[redacted]	[redacted]
$UC_4(291, 6.25)$	[redacted]	[redacted]	[redacted]

Table II.

Measured k_4 values at three time instances using four experiments, to verify the principle of superposition.

Note 12
Time constants of the step responses :

Time constant is the duration of the system's step response to reach 1-1/e $\approx$ 63.2 % of its asymptotic value. The step response data obtained for $U_1(n)$ (UC_2), provides a measure of the steady state value of the system, for a step input in u_2. This was used for computing the time-constant τ_1 = 100s of the observed exponential function. The step response data obtained for $U_2(n)$ (UC_3), provides a measure of the steady state value of the system, for a step input in u_1. This was used for computing the time-constant τ_2 = 118s of the observed exponential function.

A simple analysis reveals that, $k_4(n)$ values at three time instances for UC_4 (291 K, 6.25 J/m^2) is a sum of $k_4(n)$ values for UC_2 and UC_3. The observation for $k_4(n)$ for three time instances can be extended for the entire duration of the experiment (including steady state), thus validating the additivity property of the principle of superposition. Thus, global reticle deformation magnitude for any UC can be decomposed into the contributions of individual inputs on the overall reticle deformation. In other words, the system generates a response $(Y_1(n) + Y_2(n))$ when actuated by a signal $(U_1(n) + U_2(n))$. In fact, further analysis of the data reveals that, $k_4(n_i)$ values (where n_i is an arbitrary time instant during the experiment) when plotted on a 3-D graph, (with inputs u_1, u_2 and output k_4 representing the three orthogonal axes), for UC_1, UC_2, UC_3 and UC_4 leads to creation of a flat surface. Thus $k_4(n_i)$ value for UC_4 can be linearly predicted using $k_4(n_i)$ values of UC_1, UC_2 and UC_3. The flatness of the surface also indicates proportional relationship between the output and each individual input along both axes. Since the gradient of k_4 with respect to both inputs is constant, it leads to a flat 2-D plane in a 3-D space. This is the property of homogeneity which will be validated in the next sub-section.

Note 13
What are the boundary value inputs in the RO :

The RO can be described using a 2-D rectangular space created using orthogonal axes containing both inputs of interest, within the bounds specified in **Note 9**. Orthogonal axis for both inputs were selected to uniquely denote each UC for the RO. Boundary value inputs in the RO literally represent the UCs (step inputs) describing the edges of the rectangular space. Thus, the boundary values are the static inputs which lie at the edge of the RO shown in figure 6, along A-C-I-G-A.

3.3 Numerical analysis to demonstrate law of homogeneity

The property of homogeneity of the superposition principle states that, given a system which generates an output $Y(n)$ for an input $U(n)$, when actuated by a signal $\kappa U(n)$ would generate a signal $\kappa Y(n)$. Where κ is the gain. In other words, the dynamic relationship between input function $U(n)$ and output $Y(n)$ at any given instant n can be represented by:

$$Y(n) \propto U(n) \tag{14}$$

Which can be rewritten as.

$$Y(n) = \alpha \times U(n) \tag{15}$$

Where α is the linear proportionality constant at instant n for the dynamic system. In this subsection, a regression analysis is per-

formed using step response data to validate the consistency of α for two time instances (n_2, n_3). Since $k_4(n_i)$ is analyzed with respect to inputs $u_1(n_i)$ and $u_2(n_i)$, necessary condition for homogeneity becomes :

$$k_4(n_i) \propto (u_1(n_i), u_2(n_i)) \tag{16}$$

This can be rewritten as :

$$k_4(n_i) = \alpha \times u_1(n_i) + \beta \times u_2(n_i) \tag{17}$$

The step-response data is, collected over a duration of 2 weeks, to verify the consistency of α and β and thus validate property of homogeneity for the RHIDP model to be identified. As long as α and β are consistent throughout the RO, the output will consistently match the factor by which the input is changed. The analysis will validate the linear description of the system presented by equations 12, 13 in section 2.1. The step-response data is collected using UCs which uniformly span the entire RO. The analysis was first done using $k_4(n_3)$ values, (since n_3 closely indicates the steady state response) collected through 70 experiments, measured accurate to 2 decimal places. These values are tabulated in table XV of appendix E. This will be followed by an analysis at n_2 (an instant of transient response) to validate the property of homogeneity during the transient response of the system to step inputs.

The measured data points create a 2-D plane, in a 3-D space, illustrated in figure [redacted]. The projection of the 2-D plane on the horizontal (k_4 = 0) surface of the 3-D space represents the RO. With each point of the horizontal surface representative of individual UC. Edges of this projection area show the boundary values in RO. The $k_4(n_3)$ data collected using 70 experiments were linearly interpolated to generate the flat surface. The blue dots in the horizontal (k_4 = 0) plane represent each of the unique UCs for which $k_4(n_3)$ was measured through experiments on the metrology simulator. Nine unique points on the RO plane, along with associated $k_4(n_3)$ values, are labeled in figure [redacted] and table XV for better understanding.

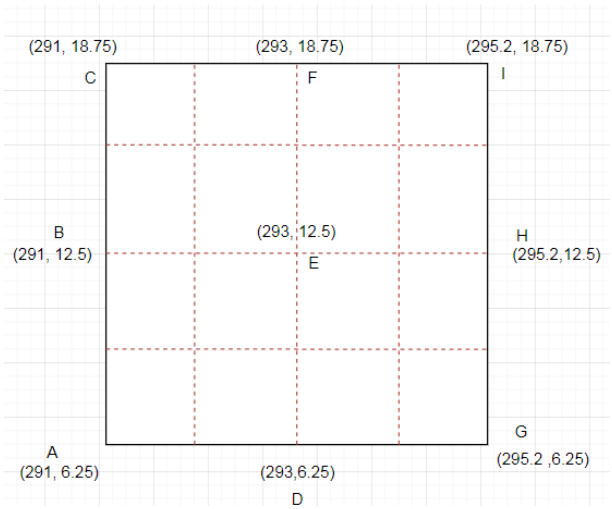

Fig. 6. Region of Operation, bifurcated into 16 spaces.

The predominantly flat nature of the linearly interpolated surface created using measured values of $k_4(n_3)$ for all UCs within the RO, illustrates the linear decoupled nature of the output with respect to both inputs for the new RHIDP model. In other words, the sensitivity of $k_4(n_3)$ with respect to both inputs, decides the gradient of the flat plane with respect to RO. The gradients of the 2-D plane measured for $k_4(n_3)$ with respect to both axes of RO; is equivalent to the proportionality constants α and β presented in equation 17. Therefore, consistent gradients of the plane with respect to both inputs, validates that the law of homogeneity holds true for the system at n_3.

Note 14
Why does the flat nature of the $k_4(n_3)$ surface indicate a decoupling of the output with respect to both inputs ?:

The 2-D surface created using $k_4(n_3)$ values validates the property of homogeneity stated in equation 17. Which shows that, the output (reticle deformation magnitude) dynamics of the system is a scaled response to the decoupled input dynamics at that instant.

The constant gradient of $k_4(n)$ with respect to both the horizontal axes at time instant n_3 (304.7 seconds), illustrated in figure [redacted], shows that, a linear prediction algorithm can be developed to predict the value of $k_4(n_i)$ for any given UC. In fact, if α and β can be computed numerically for all time instances of the experiment, $k_4(n_i)$ can also be very accurately predicted for any given UC within RO.

A regression analysis of the gradient of measured $k_4(n_3)$ values with respect to airflow temperature (α) and dose (β) is presented using tables IV, III respectively. $k_4(n_3)$ values were measured on the metrology simulator. The gradients presented in tables III , IV are computed using step response of boundary value inputs of the RO. The gradients (α) of $k_4(n_3)$ with respect to airflow temperatures, is presented in table III, step inputs in u_1 were used for various fixed step inputs in u_2, in order to determine α through a regression analysis.

Step input u_2	α - computed using step regressions in u_1 for each u_2
6.25 J/m^2	[redacted]
8.25 J/m^2	[redacted]
10.25 J/m^2	[redacted]
12.5 J/m^2	[redacted]
14.5 J/m^2	[redacted]
16.5 J/m^2	[redacted]
18.75 J/m^2	[redacted]

Table III.

Gradient of $k_4(n)$ vs airflow temperature for fixed dose values at n_3

Table above shows the computed values of α, [redacted], which amounts to 0.012% variation in α within the RO for the two-input, one-output system. The negligible variation validates the consistency of α within the entire RO. Similarly, table IV shows the computed values of β, the minimum gradient is computed [redacted]

[redacted], which amounts to an overall 0.486% variation in β within the RO for the two-input, one-output system. The negligible variation validates the consistency of β within the entire RO.

Step input u_1	β - computed using step regressions in u_2 for each u_1
291K	[redacted]
291.5K	[redacted]
292K	[redacted]
292.5K	[redacted]
293K	[redacted]
293.5K	[redacted]
294K	[redacted]
294.5K	[redacted]
295K	[redacted]
295.2K	[redacted]

Table IV.

Gradient of $k_4(n)$ vs dose for fixed airflow temperature values at n_3

It can also be inferred that, the average values of α is [redacted]. This also implies that, deformation of the reticle is more sensitive to unit variation in the airflow temperature (u_2) than, a unit variation in dose (u_1) within the RO.

Another way of accurately quantifying the consistency of α and β values, is through linear de-trending [Zhaohua Wu and Peng 2007][Estela Bee Dagum 2006] of the data set presented in table XV. De-trending of the $k_4(n_3)$ data-set leads to a magnified representation of the variations in the $k_4(n_3)$ values for different UCs, indicating the negligible variations in α and β within the RO. Table XVI in appendix E shows the residual $k_4(n_3)$ values following linear de-trending of the data-set presented in table XV.

Note 15
Why linear-detrending ?

A flat surface of $k_4(n_3)$ data-set with respect to both inputs is observed. This is also quantified through a regression analysis of the gradients of $k_4(n_3)$ with respect to both inputs in the RO. A 2-D linear de-trending of the data-set removes the best plane fit set from the data set, leaving behind the residual values. The residual values show the microscopic variation against the macroscopic linearly trending k_4 data-set.

The de-trended data-set reveals a maximum variation of 0.0289 in $k_4(n_3)$ value for the UC $292K$, $16.5J/m^2$, which is a negligible 0.05% variation in $k_4(n_3)$ over the absolute value, while minimal variation was observed for UC $292K$, $14.5J/m^2$. The de-trended $k_4(n_3)$ values are presented graphically in figure [redacted]. The figure represents the negligible variations observed per UC within the RO for the linear trending flat surface. Thus indicating variations in the proportionality constants α and β associated with the linear surface. However, the variations observed, can not conclusively be ascertained to be associated with the marginal non-linearity (in the scale of 10^-4) presented in the previous subsection, since $k_4(n_3)$ were measured accurate to within only two decimal places (10^-2). Therefore, the variations can **not** be totally associated with the system, and can be accounted to be measurement error in the $k_4(n_3)$ observations made on the metrology simulator. The negligible variation in $k_4(n_3)$ values across all UCs also verifies the consistency of α and β as presented through a regression analysis earlier in this subsection.

The regression analysis presented in this subsection using $k_4(n_3)$ data for several UCs, proves that, there exists a decoupled and linear relationship of the output with respect to both inputs for steady state, of the yet to be identified new RHIDP model within the RO. In order to extend the results of the regression analysis for any general instant n, k_4 data was also collected over 2 weeks duration for another time instant n_2 (200 seconds), n_2 is associated with transient of the system response to step inputs. The data obtained from the regression analysis for n_2 is tabulated in table V. Although only 9 $k_4(n_2)$ data points were used for validation. It is sufficient to indicate the linear relationship of the output with respect to both decoupled inputs. $k_4(n_2)$ values were measured for boundary values in the RO.

$Table$: 7			
Dose / Temp	6.25 J/m^2	12.5 J/m^2	18.75 J/m^2
291 K	[redacted] *(A)*	[redacted] *(B)*	[redacted] *(C)*
293 K	[redacted] *(D)*	[redacted] *(E)*	[redacted] *(F)*
295.2 K	[redacted] *(G)*	[redacted] *(H)*	[redacted] *(I)*

Table V.

Measured $k_4(n)$ values for 9 UCs at n_2 (200 seconds)

To verify the linear relationship, the consistency in α and β is again verified using a regression analysis. Step response data using boundary UC inputs, within RO, are considered for computing the α and β values. Table VI shows the β values computed using a regression analysis of step response data from different UCs. It can be observed that, [redacted].

Step input u_1	β - computed using step regressions in u_2 for each u_1
291K	[redacted]
293K	[redacted]
295.2K	[redacted]

Table VI.

Gradient of $k_4(n)$ vs dose for fixed airflow temperature values at n_2 (200 seconds)

The computed α values are tabulated in table VII. It can be observed that, the sensitivity of $k_4(n_2)$ with respect to airflow temperature is also consistent with an average value of [redacted].

Step input u_2	α - computed using step regressions in u_1 for each u_2
6.25 J/m^2	[redacted]
12.5 J/m^2	[redacted]
18.75 J/m^2	[redacted]

Table VII.

Gradient of $k_4(n)$ vs dose for fixed airflow temperature values at n_2 (200 seconds)

A flat 2-D surface is generated in the 3-D space for $k_4(n_2)$ similar to $k_4(n_3)$. This is shown in figure [redacted]. The analysis of $k_4(n_2)$ and $k_4(n_3)$ data shows that, homogeneity property holds true at transient, as well as steady state instances of the step response. The result can be extended for any generic time instant n_i for the new RHIDP model to be identified.

3.4 Time Invariance

In the previous two subsections, additivity and homogeneity properties of the linear system was quantified and validated using experimental data for transient and steady state values. In this sub section, the time invariant property of the system will be verified using a mathematical proof, followed by an validation using measurement data. In a mathematical sense, a dynamic system having a time-dependent input $U(n)$ and a time dependent output $Y(n)$; is considered time-invariant if a delay in it's input $U[n+c]$ directly translates into a delay of the output $Y[n+c]$.

It was already shown in equations 12, 13 that A,B and C are considered constant system matrices in the metrology simulator. To validate this result, a particular case of step input shifted by 5 RA measurements accounting for a shift of 38.78 seconds will be considered. The time shift was performed using a step input for UC_4. This is shown in [redacted]. An analysis was performed by comparing the shifted response with the un-shifted response of the system. This analysis is tabulated in table VIII. The tabulated values indicate a consistent delay of the k_4 signal over the entire experiment duration, verified using three sample points.

$Table$: 10			
k_4 (m/m)	[redacted]	[redacted]	[redacted]
System Response (s)	[redacted]	[redacted]	[redacted]
Shifted response (s)	[redacted]	[redacted]	[redacted]
Measured delay (s)	[redacted]	[redacted]	[redacted]

Table VIII.

3 k_4 values and their associated time instances for UC_4 before and after delay.

3.5 BIBO stability

Stability is a system property. BIBO stability stands for Bounded Input Bounded Output stability. Which implies that, as long as the absolute value of the input signals (u_1, u_2) is less than a certain threshold, the system is guaranteed to have a response (k_4) with an absolute value less than another threshold. In other words, there exists two constants C_1 and C_2 for a system with input $u(n)$ and output $y(n)$, such that :

$$|u(n)| < C_1 \quad \forall n \tag{18}$$

$$|y(n)| < C_2 \quad \forall n \tag{19}$$

The necessary and sufficient condition for BIBO stability of a discrete time Linear Time Invariant system is that, it's impulse response should be absolutely summable. In other words :

$$\sum_{n=-\infty}^{\infty} |h(n)| = \|h\|_1 < \infty \tag{20}$$

The impulse response $h(n)$ for the RHIDP model is shown in [redacted]. It can be deduced that, $h(n)$ is absolutely summable. Thus, the RHIDP model is also BIBO stable.

3.6 Results of the analysis :

The mathematical and numerical analysis using step-response data presented in this section points to the following results :

(1) The system doesn't satisfy the zero-input/zero-output condition. Thus has a **minimal** zero-state response. This non-linearity can be neglected.
(2) The system validates the property of additivity for transient and steady state values to step-inputs.
(3) The system validates the property of homogenity for transient and steady state values to step inputs. Thus, the principle of superposition holds true for the system, validating linear relationship between inputs u_1, u_2 and output k_4 of the system.
(4) A mathematical and numeric proof validated the time-invariant property of the system.
(5) The inputs have a decoupled effect on the reticle deformation magnitude.
(6) The system is BIBO / asymptotically stable.

The RHIDP model is thus experimentally verified to be Linear Time Invariant in nature. Consequently a linear regression modelling strategy proposed in the next sub-section for precisely predicting the temporal and spatial reticle deformation behaviour for static and low frequency dynamical inputs.

4. EXPERIMENT DESIGN

In order to perform a black-box identification, input-output data from the system needs to be collected. Reticle Align (RA) [Tripathy 2018] are instances when the deformations on the reticle surface can be measured at PARIS marks. RA occurs during interchange of wafers on the [redacted], thus a model developed around RA instances will able to accurately predict inter-wafer drifts of the measurement points on the reticle surface. RA instances are used for sampling input-output data on the metrology simulator for developing the new RHIDP model. RA occurs after the exposure of each wafer. 40 wafer exchanges are possible on the simulator, which provides 40 RA instances. The average time instant for each of the 40 RA instances on the metrology simulator is tabulated in IX. RA instances mark the sampling duration used for modelling the new MIMO RHIDP system for accounting inter-wafer drifts on the reticle surface. As such there are 40 time series input and output data-points, for

modelling the system behaviour. The LTPA algorithm explained in this paper focuses of developing a linear-regression data driven model for static and low-frequency dynamic inputs. Static inputs refer to Use Cases for the RHIDP model. Section 4.1 will delineate that, 40 RA input-output data points are sufficient for developing a precise linear regression model for predicting spatial and temporal reticle deformation for static and low frequency ($\leq$ 0.01Hz) inputs signals.

RA	*Time (s)*
1	[redacted]
2	[redacted]
3	[redacted]
4	[redacted]
5	[redacted]
6	[redacted]
⋮	⋮
20	[redacted]
⋮	⋮
40	[redacted]

Table IX.

RA instances on the metrology simulator

Prior to starting the actual identification process, choices need to be made regarding the kind of input signal to be used, it's frequency range, and the sampling rate of output data set. The data set once polished can be used for developing the RHIDP model. For accurate modelling a noise-less environment is chosen, with zero process noise. The data is directly measured from the simulator on the system, thus, limiting the measurement noise to machine precision.

4.1 Input Data-set $U(n)$

Selection of proper input signal is crucial for estimating a model. The input should be selected such that, the measured data-points at RA contain enough information regarding the excitation of the system. For example a system excited at a $U(n)$ = 0, reveals only the state trajectory of the autonomous system depending on it's initial condition, and doesn't reveal any information on the transfer from input $U(n)$ to output $Y(n)$. Therefore, for estimating a model, a non-zero signal should be provided to the system. The signal also needs to satisfy the persistency of excitation condition, which implies, the input signal should have enough frequency content in order to excite all the dominant modes of the system. A signal is therefore called persistently excited if the order of the input signal is at least greater than or equal to the system order; $i.e.$ the signal should be rich enough for precise identification of system parameters. One way of generating a persistently excited signal is to use PRBS signal, which stands for Pseudo-Random Binary Sequence, it's binary sequence with magnitude varying between 0 and 1. The rate of variation of the signal decides the order of the signal.

Due to the availability of 40 measurement instances at RA, it becomes imperative to verify whether these instances provide a sampling frequency which is rich enough for reconstructing the RHIDP model using data. Therefore, an optimal frequency range should be selected such that dominant modes of the RHIDP model (ω_B) are excited. A novel way of determining the band-width of interest (ω_B) for the system is through a step response analysis, a rule of thumb states that the sampling frequency ω_s = $10\omega_B$. It is known that, rise-time of the step response of a system approximately equals $10\omega_B$. Therefore, measuring the the rise time of the system to step responses sheds light on the bandwidth of interest (ω_B) and sampling frequency (ω_s). A simple step response analysis using UC_4 shown in [redacted] shows that the rise time of the system is approximately 182.15 seconds. Therefore, the approximate sampling frequency which is close to the bandwidth of interest ω_B, turns out to be around $\frac{1}{18.215}$ Hz. Therefore sampling the data from the system at every 18.215 seconds or faster is sufficient for reconstructing the RHIDP model from the data, since RA occurs at every 7.59 seconds, which is much smaller than 18.215 seconds, it can be concluded that RA instances provide sufficient sampling frequency for developing the data-driven model for any general dynamic input.

It is known from equation 3, that, reticle heating / cooling is a first order behaviour, therefore, it is sufficient to provide the system with a first order signal, such as a step input, which will excite the dominant system mode. The objective of the work presented in this paper revolves around developing a precise spatial and temporal prediction model for static and low frequency dynamical inputs. The LTPA prediction algorithm for static and low-frequency dynamical inputs presented in this paper shows that only 3 UCs are sufficient for calibrating the prediction model for static inputs using 40 RA measurement points. As such, step response input-output data will be the primary data of analysis for developing a precise RHIDP model.

4.1.1 ***Airflow temperature*** ***($u_1(n)$) :***. Airflow temperature (K) is one of the two inputs of interest for the new reticle deformation model, the region of operation is selected [redacted]. Note 9 provides an explanation for selecting the said input range for modelling the spatial and temporal reticle deformation behaviour

4.1.2 ***Dose / Irradiance ($u_2(n)$) :***. DUV Dose (J/m^2) is an input to the reticle and is directly related to deformations as proven in the preceding section. It represents the energy/area transmitted by deep ultra-violet (DUV) light on the reticle surface for etching the desired pattern present on the wafer. A dose [redacted] represents the range of interest for the second input u_2. Note 9 explains the reason for selecting the above range for developing the model. Since, RA instances are used for collecting the input-output data on the NTX Twinscan system. Average dose (Irradiance) between two reticle align instances (power W/m^2) is used for developing the model. An important point to note is that, the exposure area on the reticle surface is fixed and since the RA instances are uniformly spaced, irradiance (power) is a scaled value of dose (energy) for static inputs around which the RHIDP model is developed.

4.2 Output Data-set $Y(n)$:

The Output-data set plays a very important part in developing a data-driven model. Output data along with signal input data set, when sampled at appropriate frequency helps reveal the system parameters and identify precisely the transfer from input to output. The reticle deformation as measured using PARIS marks, repre-

sents the spatial and temporal deformation observed on the reticle surface. As such it is essential to decompose these two properties for developing a prediction model.

4.2.1 ***K-factor model for spatially and temporally modelling the global reticle deformation behaviour:***. k- factors were briefly discussed in 3, they provide a way to decompose spatial and temporal deformation effects seen on the reticle surface. It was also seen that $k_4(n)$ presents a direct representation of the actual reticle deformation magnitude, although $k_4(n)$ in reality represents only temporal expansion magnitude along purely y-axis, this is due to the fact that expansion effects along x-axis are affected due to lens magnification effects, and therefore k-factors other than $k_4(n)$ and $k_{18}(n)$ are not representative of the actual reticle deformation magnitude. As a consequence $k_4(n)$ signal was analyzed for establishing the Linear Time Invariant nature of the RHIDP model in section 3.

There are several challenges associated with developing RHIDP model using k-factors. These challenges are delineated below :

(1) Supposing, k- factors are used for segregating spatial and temporal behaviours, an LTI identification can only be performed using [redacted] These two k-factors are only representative of a fraction of the global reticle deformation, considering any general deformation of the reticle is **not** expected to be purely associated with spatial magnification in y effect, but rather a combination of various other spatial effects, associated with the remaining k-parameters listed in Note 5 of section 3.
(2) Due to magnification effects, none of the k-factors, except [redacted] share a linear relationship with the inputs of interest.
(3) A non-linear identification algorithm for establishing the relationship between inputs and k parameters would lead to a very complicated and non-precise temporal and consequently spatial prediction of the global reticle deformation.

Owing to the above mentioned reasons, k-factors were ruled out as possible recourse for characterizing the time-invariant, temporal deformation behaviour, of the reticle.

4.2.2 ***PARIS mark measurements for spatially and temporally modelling the global reticle deformation behaviour***. In the previous section it was established that, reticle deformation is linearly related to the inputs. Since deformations are essentially measured at [redacted] PARIS marks on the reticle. A possible alternative to k-factors, is a time series measurement of vectors representing individual PARIS mark displacements along x and y axis.

A reticle contains [redacted] PARIS marks [redacted] and [redacted] edge marks [redacted] [Tripathy 2018], combined represents a total of [redacted] measurement points (Please refer to [redacted]). Each of the [redacted] measurement vectors can be decomposed into it's components along x axis and y axis on the reticle surface, to indicate the deformations observed. Theoretically, an LTI model for identification of time domain variation of [redacted] vectors ([redacted] associated with dx and [redacted] associated with dy) can be proposed. The LTI system can be represented in the following state space form :

State equation : The equation is censored
Output equation : The equation is censored

Where,

(1) A,B are system matrices with parameters to be identified.
(2) C is a diagonal system matrix
(3) System matrix D is zero, since there is no direct feed-through between the inputs and output (Note 4)
(4) $u_i(n)$ represents both inputs of interest ($i = 1, 2$)
(5) $x_p(n)$ represents the deformation vector at PARIS mark p at instant n along x axis.
(6) $y_p(n)$ represents the deformation vector at PARIS mark p at instant n along y axis.
(7) $v_{x/y,p}(n)$ represents the output of the MIMO system at instant n along x/y axis, at PARIS mark p.

This LTI system provides a temporal prediction of deformation magnitude vectors at each PARIS mark along x and y axis. The solution of the output equation can be extended to obtain the spatial deformation ($v_p(n)$) prediction on the reticle surface using the component vectors along x and y at each PARIS mark p. The magnitude and direction of each deformation vector $v_{x/y,p}(n)$ present at [redacted] PARIS marks is given by the following relationship :

Magnitude of vector at PARIS mark p ($v_p(n)$)

$$|v_p(n)| = \sqrt{({v_{xp}}^2(n) + {v_{yp}}^2(n))} \tag{21}$$

The direction of vector at PARIS mark p ($v_p(n)$)

$$v_p(n) = tan^{-1}\left[\frac{v_{yp}(n)}{v_{xp}(n)}\right] \tag{22}$$

However, such an identification has few limitations associated with it, these are listed below :

(1) The identification requires potentially identifying ([redacted]) 1088 parameters using ([redacted]) 1280 data points, which amounts to $\approx$ 1.17 data points for each parameter, and may not be sufficient for precise identification for general dynamic input signals.
(2) LTI identification is computationally intensive and requires solving a [redacted] order system. The algorithm therefore it is not the fastest way to predict the temporal reticle deformation magnitude. Specially at ASML, which has strict requirements on processing time during photo-lithography to meet throughput expectations.

4.2.3 ***Using reticle deformation modes for developing a reduced order spatially and temporally modelling global reticle deformation behaviour***. To overcome the above mentioned shortcomings, a novel way of developing a reduced order system description, using singular value decomposition of the data-matrix, into orthonormal (spatial and temporal) basis for segregating the spatial and temporal effects of reticle deformation is proposed in the next section. This technique is related to **Multivariable Output Error State sPace** (MOESP) subspace identification algorithm explained in [Michel Verhaegen 2007]. Figure 7 shows the block-diagram representing the modelling strategy folowed in this paper.

4.3 Black-Box Identification

Subspace Identification methods are used to estimate the system matrices directly using input-output data-set. These methods are based on the fact that, by storing the input and output data in structured block Hankel matrices, it is possible to retrieve certain subspaces that are related to the system matrices of the signal generating system [Michel Verhaegen 2007]. Consequently, subspace identification algorithms help us estimate system matrices

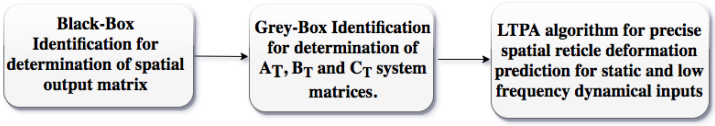

Fig. 7. Flowchart of the algorithm used for developing the Data-Driven RHIDP model for static and low frequency inputs.

A, B, C and D, which are related to the real system matrices by an unknown similarity transformation T. In other words, the estimated system matrices A_T, B_T, C_T and D_T are related to the system matrices A, B, C and D of the signal generating model by the following relationships :

$$A_T = T^{-1}AT,\ B_T = T^{-1}B,\ C_T = CT,\ D_T = D.$$

UCs are important class of inputs for the RHIDP model, and essentially represents step inputs to the system. In this section, a novel linear regression algorithm is proposed for precise identification of global reticle deformation for various static inputs (UCs) and low frequency dynamic inputs. It has already been shown that, the direct feed-through from input to the output for the RHIDP model is zero (Note 6). The Linear Temporal Prediction Algorithm (LTPA) will be used for estimating system matrices A, B and C up to an unknown similarity transformation. It was shown in section 3.4, the state of a system 12, 13, with initial state $x(0)$, at time instant n is given by :

$$x(n) = A^n x(0) + \sum_{i=0}^{n-1} A^{n-i-1} B u(i) \tag{23}$$

In order to identify the transfer parameters from inputs to output (reticle deformation), using equation 13, the following relationship between the input and output data-sequence is obtained :

$$y(n) = Cx(n) \tag{24}$$

4.3.1 ***Estimating spatial output matrix ϕ_T for developing the RHIDP model for static and low frequency input signals***. :

It is known that the direct feed-through from inputs to spatial reticle deformation is zero. The system matrices are time-invariant, with initial state $x(0)$. A singular value decomposition separates the spatial orthonormal basis from the temporal orthonormal basis connected by a similarity transformation. The SVD of step response data directly generates the output trajectory for a given Use Case, which is used for developing the final RHIDP model using the Linear Temporal Prediction Algorithm (LTPA).

Observations / Knowledge:

(1) It is known that the direct feed-through (System Matrix D) from the inputs to output is zero.

(2) It is also known that each measurement $y(n)$ represents vector containing the spatial distribution of deformation for all [redacted] PARIS marks at instant n, and it becomes important to separate the temporal and spatial behaviour, to develop a LTI prediction algorithm.

(3) The presence of only 40 measurements points limits the size of $Y_{0,s,N}$

Note 16

[redacted]

$$C^n = \mathcal{R}(G)^T \bigoplus \mathcal{N}(G) \tag{25}$$

$$C^m = \mathcal{R}(G) \bigoplus \mathcal{N}(G)^T \tag{26}$$

[redacted]

$$\begin{bmatrix}\mathcal{U}_\mathcal{R} & \mathcal{U}_\mathcal{N}\end{bmatrix} \begin{bmatrix} \sigma_1 & 0 & 0 & \dots & 0 & 0 \\ 0 & \sigma_2 & 0 & \dots & 0 & 0 \\ \vdots & \vdots & \ddots & \dots & \dots & \vdots \\ 0 & 0 & \dots & \sigma_p & 0 & 0 \\ 0 & 0 & 0 & \dots & 0 & 0 \\ 0 & 0 & 0 & \dots & 0 & 0 \end{bmatrix} \begin{bmatrix}\mathcal{V}_\mathcal{R} \\ \mathcal{V}_\mathcal{N}\end{bmatrix} \tag{27}$$

$$\begin{bmatrix}u_1 & \dots & u_p & u_{p+1} \dots u_m\end{bmatrix} \begin{bmatrix} S_{p\times p} & 0 \\ 0 & 0 \end{bmatrix} \begin{bmatrix} v_1 \\ \vdots \\ v_p \\ v_{p+1} \\ \vdots \\ v_n \end{bmatrix} \tag{28}$$

[redacted]

$$\sigma_1 \geq \sigma_2 \geq \dots \geq \sigma_p > 0 \tag{29}$$

[redacted]

$$S = \textbf{diagonal}(\sigma_1, \sigma_2, \dots, \sigma_p) \in \mathbb{R}^{p\times p}. \tag{30}$$

[redacted]

The column vectors form spans for the subspaces:

$$\mathcal{R}(G) = span\{u_1 \dots u_p\} \tag{31}$$

$$\mathcal{R}(G)^T = span\{v_1 \dots v_p\} \tag{32}$$

$$\mathcal{N}(G)^T = span\{u_{p+1} \dots v_m\} \tag{33}$$

$$\mathcal{N}(G) = span\{v_{p+1} \dots v_n\} \tag{34}$$

With the knowledge at hand, a data equation created by stacking time shifted outputs vectors next to each other using equation 24 is considered, this converges the data-equation to the form :

$$\begin{bmatrix}y(0) & y(1) & \cdots & y(N-1)\end{bmatrix} = CX_{0,N} \tag{35}$$

Where,

$$X_{0,N} = [x(0)\ \ x(1)\ \ \cdots x(N-1)] \tag{36}$$

Rewriting equation 35, to represent spatial and temporal data, the following relationship is obtained :

This equation is censored.

This is a very important relationship, as it shows that, the spatial distribution of the output deformation matrix lies in the range space of time independent ϕ_T matrix. Where ϕ_T is related to output matrix C presented in equation 35 through a similarity transformation T. In other words, the data matrix can be factorized into a time independent C matrix and and a time dependent $X_{0,\blacksquare,N}$ matrix. For N = 40 (40 RA measurement instances), the above relationship converges to the equation ■. The arrangement of the features in the data-set presented in equation ■ is important, it can be seen that "**feature one**" describing deformation vectors along x and y axis on the reticle surface are arranged vertically for every time instant n. While "**feature two**" describing the temporal variation in magnitude associated with the spatial description given by "feature one" is arranged horizontally for increasing time instances.

This equation is censored.

Singular Value Decomposition (SVD) is a very powerful statistical tool which determines the correlation between the orthonormal basis describing both features of the data-set. The singular values indicate the relative co-variance between each pair of orthonormal basis determined by SVD. In a compact notation the data equation ■ can be written in the following way :

$$Y_{0,\blacksquare,40} = \phi_T X_{0,\blacksquare,40} \tag{37}$$

In other words, Singular value decomposition of $Y_{0,\blacksquare,40}$ presents a linear transformation taking a vector v_1 in its row space (**feature one**) to a vector $u_1 = Y_{0,\blacksquare,40} v_1$ in its column space (**feature two**). The SVD arises from finding an orthogonal basis for the row space that gets transformed into an orthogonal basis for the column space: $Y_{0,\blacksquare,40} v_i = \sigma_i u$. [Strang 2011]. Considering the RHIDP model is developed for precise prediction of global reticle deformation for various static and low frequency input signals. A **nominal** step input excitation signal using UC_4 is provided to the system for analysis of row and column spaces of obtained data-matrix $Y_{0,\blacksquare,40}$, The analysis will reveal insightful information regarding dominant modes obtained for each orthonormal u_i and v_i basis which relate both features present in the data-matrix. SVD of the $Y_{0,\blacksquare,40}$ allows determination of the column space of $Y_{0,\blacksquare,40}$. [Michel Verhaegen 2007]. This concept was obtained from [Kant 2018]. Singular Value Decomposition of $Y_{0,40}$, produces the following factorization :

$$Y_{0,\blacksquare,40} = \bigcup_{\blacksquare\times\blacksquare} \cdot \sum_{\blacksquare\times 40} \cdot \bigvee^{T}_{40\times 40} \tag{38}$$

Where $\bigcup_{\blacksquare\times\blacksquare}$ consists of orthonormal basis vectors

4.3.2 ***Reduced Model Order Selection***. The singular value plot shown in figure 8 indicates the dominant modes excited for "nominal" UC_4 (291,6.25). Although it's difficult to differentiate the system order looking at the gaps in the singular value, the first 14 dominant modes represent the significant singular values among ■ possible modes. However, for developing the **reduced order** system description for the RHIDP model, the first 5 modes are considered, since these modes contribute to deformation effects of magnitude sufficient for developing an accurate prediction model for static and low frequency dynamic input signals. In other words, these singular values are associated with the most variance in the deformation magnitudes. Consequently, selection of the first five modes among the ■ modes represents a reduction in the order of the system ■ presented in section 4.2.2.

Note 17
Percentage of variation explained by each SVD mode:

If the singular value decomposition of a matrix G is given by :

$$G = \bigcup \sum \bigvee^{T} \tag{39}$$

The amount of overall variance expound by the i^{th} pair of orthonormal SVD vectors ("i^{th} mode") is given by :

$$s^2 = \frac{\|u_i \sigma_i v_i^T\|^2}{\|G\|^2} = \frac{\sigma_i^2}{\sum_j \sigma_j^2} \tag{40}$$

where, σ_j are singular values (diagonal of matrix $\sum$). u_i and v_i are the orthonormal basis vectors associated with mode i. All norms are Frobenius norms.

The amount of variance expound by i^{th} mode of k^{th} column, where g_k is the k^{th} column of G is given by :

$$s^2 = \frac{\|u_i \sigma_i v_{i,k}^T\|^2}{\|g_k\|^2} = \frac{\sigma_i^2 v_{i,k}^2}{\|g_k^2\|^2} \tag{41}$$

Note 18
SVD and physical interpretation of $\bigcup$ and $\bigvee^T$ data-set:

In machine learning and statistics, Singular Value Decomposition is known for extracting insightful information from any data matrix, [Modarresi 2005] in particular, a singular value decomposition is known for factorizing a matrix to reveal it's constituent rotation and scaling matrices [Pisani 2015][Marschner 2010][Olga Sorkine-Hornung 2017]. These rotation / scaling matrices in general contain predominant features of interest present in the data-set.

The data-set $Y_{0,1,40}$ which is factorized using a Singular value Decomposition contains spatial as well as temporal data arranged along vertical and horizontal axes of the matrix. As such SVD factorization helps separate these two properties by placing them in orthogonal matrices $\bigcup_n$ and $\bigvee_n{}^T$, which basically contain the mode shapes and modal magnitude. Mode shapes contain the spatial reticle deformation vectors in the identified ϕ_T system matrix, whereas the data encapsulating the temporal variations in the mode-shape is contained in $X_{0,N,40}$ data-set ($\sum_n \cdot \bigvee_n{}^T$). This data is used to determine modal transfer functions. [J. B. Fahnline and Shepherd 2017].

■ shows the five most dominant modes and their contribution to the global reticle deformation with respect to time. The maximum contribution to the deformation magnitude of the least dominant (5^{th}) mode selected for developing the RHIDP model is in the scale of 10^{-11} m. The contribution of the remainder $(\blacksquare - 5)$ modes is negligible and is thus more than sufficient for accounting all variances less than nanometers (10^{-9}) m in the deformation magnitude as desired from the prediction model to be used for lithography. Tables X, XI, XII tabulate the VAF % as a function of increasing modal contributions for ■.

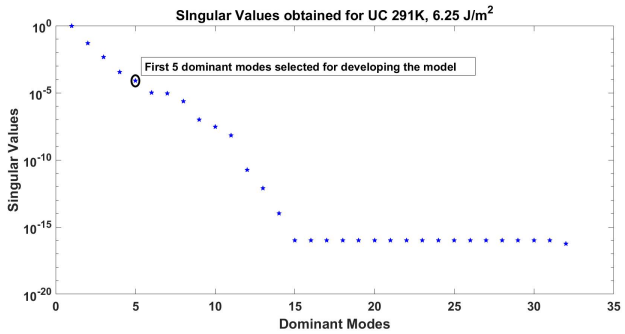

Fig. 8. Singular Values from deformation data for the nominal step input UC $291K, 6.25\ J/m^2$

VAF is a metric used for assessing the quality of model. It is defined by :

$$\text{VAF(y(n)}, y(\hat{n})) = max(0, 1 - \frac{\frac{1}{N}\sum_{n=1}^{N} \|y(n) - y(\hat{n})\|_2^2}{\frac{1}{N}\sum_{n=1}^{N} \|y(n)\|_2^2}.100\%) \quad (42)$$

Where, y is the signal from the signal generating model and $\hat{y}$ is the predicted (deformation magnitude) signal, n is the sample index and N is the number of samples. The signal $\hat{y}$ is determined as a function of modal magnitude as specified in equation 40. For example, $\hat{y}$ values for first mode helps determine the predicted $\|v_p\|$ for each paris and edge mark specified in equation 21, through a linear combination with the associated mode-shape (spatial output matrix). In other words, $\|v_p\|$ using the first mode is determined in the following way:

$$v_{(x/y),p}(t)_1 = \sum_{i=1}^{1} \phi_T(x,y).\eta(t)_i \quad (43)$$

Similarly, $\hat{y}$ values as a function of the first three modes is computed in the following way:

$$v_{(x/y),p}(t)_3 = \sum_{i=1}^{3} \phi_T(x,y).\eta(t)_i \quad (44)$$

Where ϕ_T contain the mode-shapes obtained using the SVD. This is elaborated later in this subsection. VAF presents values between 0% to 100 %. Higher the VAF, lower is the prediction error, better is the modeled system.

VAF %	[redacted]	[redacted]	[redacted]	[redacted]	[redacted]
Mode 1	99.7055	99.9121	99.9924	99.9919	99.9530
Mode 2	99.9929	99.9985	99.9999	99.9982	99.9971
Mode 3	99.9999	99.9999	99.9999	99.9999	99.9999
Mode 4	99.9999	99.9999	99.9999	99.9999	99.9999
Mode 5	99.9999	99.9999	99.9999	99.9999	99.9999
Mode 6	99.9999	99.9999	99.9999	99.9999	99.9999

Table X.

VAF for the [redacted] as a function of increasing modes

VAF %	[redacted]	[redacted]	[redacted]	[redacted]	[redacted]
Mode 1	99.8974	99.8257	99.7354	99.3482	99.7143
Mode 2	99.9982	99.9993	99.9892	99.8376	99.9937
Mode 3	99.9999	99.9999	99.9998	99.9976	99.9999
Mode 4	99.9999	99.9999	99.9999	99.9999	99.9999
Mode 5	99.9999	99.9999	99.9999	99.9999	99.9999
Mode 6	99.9999	99.9999	99.9999	99.9999	99.9999

Table XI.

VAF for PARIS [redacted] and Edge marks [redacted] as a function of increasing modes

VAF %	[redacted]	[redacted]	[redacted]	[redacted]	[redacted]	[redacted]
Mode 1	99.9168	99.9938	99.9906	99.9498	99.8929	99.8199
Mode 2	99.9989	99.9998	99.9977	99.9966	99.9978	99.9993
Mode 3	99.9999	99.9999	99.9999	99.9999	99.9999	99.9999
Mode 4	99.9999	99.9999	99.9999	99.9999	99.9999	99.9999
Mode 5	99.9999	99.9999	99.9999	99.9999	99.9999	99.9999
Mode 6	99.9999	99.9999	99.9999	99.9999	99.9999	99.9999

Table XII.

VAF for the [redacted] PARIS Marks as a function of increasing modes

The determined mode-shapes containing the spatial description of reticle deformation associated with the five most dominant modes are presented using figures 10, 11, 12, 13 and 14 in Appendix-F. If $\Sigma_r \in R_{r\times r}$ and rank(Σ_r) = r, then, the mode-shapes contained in $\bigcup_{[redacted]\times r}$ can be denoted by :

$$\bigcup_{[redacted]\times r} = \phi_T \quad (45)$$

Although it can be seen from the VAF % values, the first mode accounts for 99 % of the overall deformation magnitude variances. VAF % do not necessarily give an indication of the desired accuracy for the RHIDP model. Note 17 expresses that, higher the number of modes used for developing the prediction model, higher would be the accuracy of prediction by the model. This can also be seen from the VAF values presented in tables X, XI, XII. Considering the precision requirements from the RHIDP model, first 5 modes are selected for developing the model. This is also indicated in the singular value plot shown in figure 8. Consequently, equation 45 converges to the following :

$$\bigcup_{[redacted]\times 5} = \phi_T \quad (46)$$

Therefore SVD helps determine ϕ_T, which contains the orthonormal basis describing the range space of spatial deformation, up to an unknown similarity transformation T. An important point to note is that, choosing $\bigcup_5 \sum_5^{1/2}$ instead of $\bigcup_5$, would lead to determination of the spatial output matrix ϕ_{T_1} instead of ϕ_T, which would be related to the spatial output matrix ϕ of the signal generating model with an unknown similarity transformation T_1, instead of T. Therefore the choice of system matrix to be equal to $\bigcup_5$ is arbitrary. However for the identification of the RHIDP model, the five columns of left singular orthogonal vectors $\bigcup_5$ are selected for determining the spatial output matrix ϕ_T. Consequently, for the RHIDP model, $X_{0,40}$ data is the product of the singular values and right singular orthogonal vectors $\left[\sum_{5\times 5} \bigvee_{5\times 40}{}^T\right]$, given by :

$$\left[\sum_{5\times5}\bigvee_{5\times40}\right]^T = X_{0,5,40} = \begin{bmatrix} x(0) & x(1) & \cdots x(39) \end{bmatrix} \quad (47)$$

4.3.3 ***Determination of A_T, B_T and C_T system matrices for static inputs***. The singular value decomposition of the output data-matrix was used for determination of the orthonormal basis vectors describing the spatial description of reticle deformation (ϕ_T) and the orthonormal basis vectors describing the temporal description for a the nominal step input signal. It was shown that the global temporal and spatial reticle deformation behaviour lies in the range space of ϕ_T. The temporal data obtained following the singular value decomposition will be used for Linear Temporal Prediction Algorithm (LTPA) developed for static and low frequency input signals explained in section 4.4. It is known from equation 23, the state trajectory when excited by a external signal u is given by the following relationship :

$$x(n) = {A_T}^n x(0) + \sum_{i=0}^{n-1} {A_T}^{n-i-1} B_T u(i) \quad (48)$$

It can be deduced that, the function describing the output data $X_{0,5,40}$ can be described by the state trajectory 48 as long as the the output C_T matrix describing the temporal behaviour doesn't include any scaling terms and is used for linearly adding the decoupled state sequences $X_{0,5,40}$ obtained for each input. In other words output system matrix C which is related to the similarity transformed output matrix C_T can be expressed using the following relationship :

$$X_{0,5,40} = \begin{bmatrix} 1 & 1 \end{bmatrix} \begin{bmatrix} \{X_{0,5,40}\}_{u_1} \\ \{X_{0,5,40}\}_{u_2} \end{bmatrix} \quad (49)$$

In other words,

$$X_{0,5,40} = \begin{bmatrix} C_T \end{bmatrix} \begin{bmatrix} \{X_{0,5,40}\}_{u_1} \\ \{X_{0,5,40}\}_{u_2} \end{bmatrix} \quad (50)$$

Where, $\{X_{0,5,40}\}_{u_1}$ and $\{X_{0,5,40}\}_{u_2}$ are the state-trajectory data obtained for static inputs u_1 and u_2. Considering the system was excited using a step input, the relation of the obtained state data ($\{X_{0,5,40}\}_{u_1}$ and $\{X_{0,5,40}\}_{u_2}$) with system matrices A_T and B_T, is given by plugging in values of n = (0 to 39) in the equation 48, with $u_1(n)$ and $u_2(n)$ = 1 (or scaled version thereof, depending on UC), gives the following relationship :

$$X_{0,5,40} = \Big[x(0), A_T x(0) + B_T \begin{bmatrix} u_1(1) \\ u_2(1) \end{bmatrix}, \cdots \quad (51)$$

$${A_T}^2 x(0) + (A_T B_T + B_T) \begin{bmatrix} u_1(2) \\ u_2(2) \end{bmatrix}, \cdots$$

$${A_T}^{40} x(0) + ({A_T}^{39} B_T + \cdots + A_T B_T + B_T) \begin{bmatrix} u_1(3) \\ u_2(3) \end{bmatrix} \Big]$$

$x(0)$ can be determined directly by reading off the first 5×1 elements of the sequence presented in the equation 47. However, considering the combination of A_T and B_T matrices present in the state-trajectory $X_{0,5,40}$ described by equation 51, determination of system matrices A_T and B_T from the data for static inputs is not very straight forward. Therefore a Grey-box identification strategy for determination of the system matrices A_T, B_T and C_T using curve fitting is proposed in section 4.4 to the reader.

4.4 Grey-Box Identification

It is known that, D_T = 0, having computed C_T, a grey box identification using curve fitting of the $X_{0,5,40}$ data-set presented in equation 47 is another approach for determination of A_T and B_T system matrices. The algorithm is presented in this section.

4.4.1 ***Estimating A_T and B_T through curve fitting of $X_{0,i,n}$ data-set for temporal prediction***. :

The function describing the reticle heating curve for any UC, with mode i and unique UC setting j can be described using the following relationship :

$$\eta(t)_{i,j} = {u_1(t)}_j \{ {\kappa_1}^{i,j} (1 - e^{\frac{-t}{{\tau_1}^{i,j}}}) \} + {u_2(t)}_j \{ {\kappa_2}^{i,j} (1 - e^{\frac{-t}{{\tau_2}^{i,j}}}) \} \quad (52)$$

Where,

(1) ${u_1(t)}_j$ is the airflow temperature associated with the unique use case j.

(2) ${u_2(t)}_j$ is the dose (scaled irradiance for static inputs) associated with the unique use case j.

(3) κ_1 is a RH parameter. It is associated with mode i, and use case j. It encompasses the sensitivity of the mode i with respect to airflow temperature.

(4) κ_2 is second RH parameter. It is associated with mode i, and use case j. It encompasses the sensitivity of the mode i with respect to dose.

(5) τ_1 and τ_2 are the third and fourth RH parameters, representing time constants associated with the function describing RH for mode i and use case j, with respect to airflow temperature and dose respectively.

Each reticle heating mode can be described using the state space form [Kant 2015] :

$$\begin{bmatrix} \dot{x}_1(t) \\ \dot{x}_2(t) \end{bmatrix}_{i,j} = \begin{bmatrix} -\frac{1}{\tau_1} & 0 \\ 0 & -\frac{1}{\tau_2} \end{bmatrix} \begin{bmatrix} x_1(t) \\ x_2(t) \end{bmatrix}_{i,j} + \begin{bmatrix} \frac{{\kappa_1}^{i,j}}{\tau_1} & 0 \\ 0 & \frac{{\kappa_2}^{i,j}}{\tau_2} \end{bmatrix} \begin{bmatrix} {u_1(t)}_j \\ {u_2(t)}_j \end{bmatrix} \quad (53)$$

The output equation of the state dynamics is given by :

$$\eta(t)_i = \begin{bmatrix} 1 & 1 \end{bmatrix} \begin{bmatrix} x_1(t) \\ x_2(t) \end{bmatrix}_{i,j} \quad (54)$$

Equation 54 indicates a linear addition of orthogonal state prediction vectors for mode i and UC j.

Note 19
Transfer function and stability:

The transfer function relating signal $\eta_i(t)$ with airflow temperature $u_1(t)$ and dose $u_2(t)$ (Scaled Irradiance) for a given state order i, is given by :

$$\eta(s) = \frac{\frac{\kappa_1}{\tau_1}}{s + \frac{1}{\tau_1}} u_1(s) + \frac{\frac{\kappa_2}{\tau_2}}{s + \frac{1}{\tau_2}} u_2(s) \tag{55}$$

The poles of the system associated with mode i lie at $(-\frac{1}{\tau_1}, 0)$ and $(-\frac{1}{\tau_2}, 0)$ on the s plane. Where, τ_1 and τ_2 are time constants associated with the function describing mode i. The time constants of each of the function, irrespective of the mode i is a positive number. Consequently, all the poles of the system lie on the left half of the s plane, verifying the asymptotic stability of the system presented to the reader in section 3.5.

The system matrices associated with equations 53 and 54 can be represented by $A_{i,j}$, $B_{i,j}$ and $C_{i,j}$ for mode i and UC j. $x_{i,j}(t)$ represents the state dynamics associated with mode i and UC j.

A complete linear state description of the RHIDP model, can be developed, by combining all the states associated with higher modes in a single state space model. Since the first five modes were selected for modelling, the state space description is given by :

$$\dot{x}_j = \begin{bmatrix} A_{1,j} & 0 & \cdots & \cdots & 0 \\ 0 & A_{2,j} & 0 & \cdots & 0 \\ 0 & 0 & A_{3,j} & \cdots & 0 \\ \vdots & \vdots & \ddots & \vdots & \\ 0 & 0 & \cdots & \cdots & A_{5,j} \end{bmatrix} x_j + \begin{bmatrix} B_{1,j} \\ B_{2,j} \\ B_{3,j} \\ \vdots \\ B_{5,j} \end{bmatrix} \begin{bmatrix} u_1 \\ u_2 \end{bmatrix}_j \tag{56}$$

$$\eta_j = \begin{bmatrix} C_{1,j} & 0 & \cdots & 0 \\ 0 & C_{2,j} & \cdots & 0 \\ \vdots & \vdots & \ddots & \vdots \\ 0 & 0 & 0 & C_{5,j} \end{bmatrix} x_j \tag{57}$$

With an equivalent representation of the form :

$$\dot{x}_j = A_T x_j + B_T \begin{bmatrix} u_1 \\ u_2 \end{bmatrix}_j \tag{58}$$

$$\eta_j = C_T x_j \tag{59}$$

Where,

(1) A_T, B_T and C_T are the system matrices of the identified RHIDP model known upto an unknown a simillarity transformation T.
(2) η_j is a continuous time function representative of the discrete time state sequence $X_{0,5,40}$ obtained from singular value decomposition presented in section 4.3.
(3) x_j encompasses the decoupled states associated with inputs u_1 and u_2 for each mode i = 1 to 5, for static input UC j.

The above description represents the dynamics of the RH model for a certain use case j, within the region of operation. The system matrices associated with equations 56 and 57 represent the system matrices A_T, B_T and C_T of the identified RHIDP model upto an unknown similarity transformation T. The temporal modal magnitude prediction results obtained from equation 57, represents the data along the transformed orthogonal basis V^T. It is known that the spatial description of the global reticle deformation lies in the range space of ϕ_T. The spatial and temporal description of the reticle deformation behaviour is thus obtained by recombining the modal temporal data described using the function η_T with mode shapes contained in ϕ_T (equation 46). This is shown using the following relationship :

$$v_{(x/y),p}(t) = \sum_{i=1}^{5} \phi_T(x, y).\eta(t)_i \tag{60}$$

Where,

(1) $v_{(x/y),p}(t)$, represents the spatial and temporal global reticle deformation prediction vectors along x and y axes at PARIS mark p.
(2) $\phi_T(x, y)$ is the time independent spatial output matrix of the signal generating model known upto a simillarity transformation T. It contains dominant the orthogonal basis describing the mode-shapes which represent the spatial description of reticle deformation.
(3) $\eta(t)$ is the modal magnitude prediction function.
(4) i represents first five dominant modes of the system.

Magnitude of predicted vector at PARIS mark p ($v_p[t]$)

$$|v_p[t]| = \sqrt{({v_{xp}}^2[t] + {v_{yp}}^2[t])} \tag{61}$$

The direction of predicted vector at PARIS mark p ($v_p[t]$)

$$v_p[t] = tan^{-1}\left[\frac{v_{yp}[t]}{v_{xp}[t]}\right] \tag{62}$$

Equations 53 and 54 showed that, each modal magnitude is represented using a second order system, thus the RHIDP model requires 5 × 2 = 10^{th} order state space description for precise reticle deformation prediction. Each mode is associated with identification of four unknown parameters, namely τ_1, τ_2, κ_1 and κ_2. Therefore, an identification of 4 × 5 = 20 parameters (parameters per mode × number of modes) would be required for every UC. The LTPA presented to the reader in the next sub-section performs a linear prediction of lumped-static parameters using linear least-squares. LTPA will be used for precise spatial and temporal prediction of Reticle deformation for various UCs.

4.5 Linear Temporal Prediction Algorithm (LTPA) for any UC within RO

The dynamics of mode i and UC j was represented using the following relationship :

$$\eta(t)_{i,j} = u_1(t)_j\{{\kappa_1}^{i,j}(1 - e^{\frac{-t}{{\tau_1}^{i,j}}})\} + u_2(t)_j\{{\kappa_2}^{i,j}(1 - e^{\frac{-t}{{\tau_2}^{i,j}}})\} \tag{63}$$

Each of the unique parameters τ_1, τ_2, κ_1 and κ_2 is dependent on the mode for which the curve is estimated. In this sub-section, a novel linear regression algorithm for precisely estimating the spatial and temporal deformations of the reticle for various UCs within

RO is explained to the reader. The regression model also estimates reticle deformation for low frequency input signals. Considering the limited number of available data-points, the LTPA is one of the optimal approaches for estimating reticle deformation for various static inputs (UC) using only three data-points. To this end, the sensitivity of $\eta_{i,j}(t)$ with respect to decoupled inputs u_1 and u_2 is determined for mode i and Use Case j. The relationship of the temporal dynamics of each mode i, with respect to both inputs (sensitivity) is given below :

$$\frac{\partial \eta(t)_i}{\partial u_1}|_{(u_2=6.25)} = \kappa_1^i(1 - e^{\frac{-t}{\tau_1{}^i}}) = P_1(t) \tag{64}$$

$$\frac{\partial \eta(t)_i}{\partial u_2}|_{(u_1=291)} = \kappa_2^i(1 - e^{\frac{-t}{\tau_2{}^i}}) = P_2(t) \tag{65}$$

Note 20
Optimization Algorithm for estimating lumped parameters:

Equation 63 can be rewritten as :

$$\eta(t)_{i,j} = u_1(t)_j P_1 + u_2(t)_j P_2 \tag{66}$$

Using the measured sequence of output $\eta(t)_{i,j}$, inputs $u_1(t)_j$ and $u_2(t)_j$ at RA instances, static parameters P_1 and P_2 of equation 66 for each mode i can be estimated using a least squares approach by using 3 data-points (Use Cases) for the linear system in the following way :

[redacted] (67)

[redacted] (68)

Subtracting equation 67 obtained for first UC from 68 obtained for second UC, we obtain the following relationship :

[redacted] (69)

Equation 69 can be re-written as :

[redacted] $= P_1$ (70)

for estimating parameter P_1.
Similarly parameter P_2 can be estimated using a third UC. This is explained below :

[redacted] (71)

Subtracting equation 67 obtained for first UC from 71 obtained for third UC, we obtain the following relationship :

[redacted] (72)

Equation 72 can be re-written as :

[redacted] $= P_2$ (73)

for estimating parameter P_2.

η_i obtained for UC 291,6.25 is chosen as the nominal function describing the heating dynamics of the reticle. The LTPA algorithm is developed around this nominal input. The reason for selecting u_1 = 291 K and u_2 = 6.25 J/m^2 is arbitrary, another UC within RO can also be chosen as the nominal input for predicting the dynamics using the LTPA. The step response analysis using the k-factor model presented to the reader in section 3 indicated a linear relationship of the temporal reticle deformation magnitude with respect to decoupled inputs. The LTPA uses relationships 74 and 75 for precisely predicting the state trajectory $x_i(t)$ of the system for a given input combination $u_1(t)$ and $u_2(t)$ at time t using the sensitivities determined in equations 64 and 65.

$$\frac{\partial x_1(t)_{i,j}}{\partial t} = x(t)_{(i,j=291,6.25)} + \{u_2 - 6.25\} \times \frac{\partial \eta(t)_i}{\partial u_2}|_{(u_1=291)} \tag{74}$$

$$\frac{\partial x_2(t)_{i,j}}{\partial t} = x(t)_{(i,j=291,6.25)} + \{u_1 - 291\} \times \frac{\partial \eta(t)_i}{\partial u_1}|_{(u_2=6.25)} \tag{75}$$

$$\eta(t)_{i,j} = \begin{bmatrix} 1 & 1 \end{bmatrix} \begin{bmatrix} x_1(t) \\ x_2(t) \end{bmatrix}_{i,j} \tag{76}$$

Where,

(1) $x(t)$ is the predicted modal magnitude with respect to time.
(2) i is the predicted mode.
(3) u_1 is the step input in airflow temperature of the predicted UC.
(4) u_2 is the step input in dose of the predicted UC.
(5) j is the UC associated with step inputs u_1 and u_2 used for predicting $\eta(t)$ within RO.

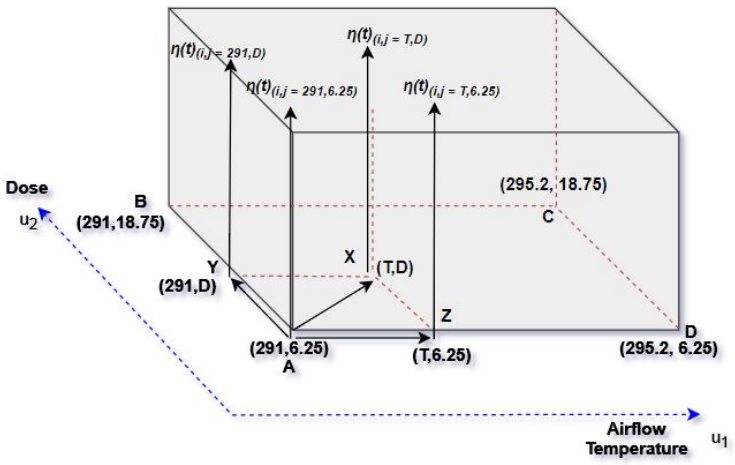

Fig. 9. Graphical Interpretation of LTPA

4.5.1 ***Graphical interpretation of LTPA***. A graphical interpretation of the LTPA is presented in this sub-section. The interpretation will help the reader develop a better understanding of equations 64 , 65 describing the static sensitivities and state equation 74 and 75. Considering the decoupled nature of inputs u_1 and u_2

with respect to reticle heating modes η_i, a 3-D visualization of the LTPA is presented to the reader using figure 9. The A-B-C-D plane is used to represent the RO for the RHIDP model with orthogonal axes of RO illustrative of step input values in u_1 and u_2. The vertical axis of the figure indicates the state trajectory $x_i(t)$ for a given UC. In particular the state trajectory for UC A on the RO is used as the **nominal** $x_i(t)$ for the LTPA. This novel algorithm is used for predicting $\eta_i(t)$ which is a linear combination of the states $x_i(t)$. The **nominal** states $x_i(t)$ (i = 1,2,3,4,5) are illustrated in [redacted]. Similarly [redacted] illustrate the state sequences obtained for UCs B,C and D of the RO.

The analysis reveals that, the temporal magnitude of each mode i is linearly proportional to the UC in question. In fact η_i for any UC within RO can be predicted using a linear prediction algorithm by computing the sensitivity of η_i with respect to decoupled inputs u_1 and u_2. The linearity is verified through a regression analysis (in the lines of section 3.2) by randomly selecting two time instances at 20^{th} RA instant and 40^{th} RA instant. η_1 values for 12 uniformly spaced UCs within RO are measured and interpolated. The interpolated data points generate a flat 2-D surface in a 3-D space. Tabulated η_1 values at 20^{th} RA instant are labeled and presented in table XIII and it's associated interpolated surface is shown in figure [redacted]. Similarly, tabulated η_1 values for 40^{th} RA instant are labeled and presented in table XIV and it's associated interpolated surface is shown in figure [redacted].

$Table: 15\ (\times 10^{-07})$			
Dose / Temp	6.25 J/m^2	12.5 J/m^2	18.75 J/m^2
291 K	[redacted] *(A)*	[redacted] *(B)*	[redacted] *(C)*
292.5 K	[redacted] *(D)*	[redacted] *(E)*	[redacted] *(F)*
294 K	[redacted] *(G)*	[redacted] *(H)*	[redacted] *(I)*
295.2 K	[redacted] *(J)*	[redacted] *(K)*	[redacted] *(L)*

Table XIII.

Measured η_1 at 20^{th} RA instant for 12 uniformly spaced UCs

$Table: 16\ (\times 10^{-07})$			
Dose / Temp	6.25 J/m^2	12.5 J/m^2	18.75 J/m^2
291 K	[redacted] *(A)*	[redacted] *(B)*	[redacted] *(C)*
292.5 K	[redacted] *(D)*	[redacted] *(E)*	[redacted] *(F)*
294 K	[redacted] *(G)*	[redacted] *(H)*	[redacted] *(I)*
295.2 K	[redacted] *(J)*	[redacted] *(K)*	[redacted] *(L)*

Table XIV.

Measured η_1 at 40^{th} RA instant for 12 uniformly spaced UCs

The flatness of the generated surface indicates consistency in the sensitivity (equations 64 and 65) of η_i with respect to inputs u_1 and u_2 for any given time instant t. This experimental result can be extended to all modes (i = 2,3,4,5). Consequently, the temporal RH effect for any UC within RO can be precisely estimated using a linear prediction of all the associated modes.

4.6 Results of LTPA for Various Static and Dynamic Inputs in RO

In the previous section, computing the sensitivity of $\eta_i(t)$ with respect to decoupled static inputs u_1 and u_2 using measured $\eta_i(t)$ values for UCs A, Z and Y using a least squares prediction of static parameters was illustrated. Z and Y stand for static data-points for UCs - (292, 6.25) and (291, 8.25). The choice of UCs Z and Y for computing sensitivities along inputs u_1 and u_2 was arbitrary since it is proven that modal sensitivities $\frac{\partial \eta(t)_i}{\partial u_1}$ and $\frac{\partial \eta(t)_i}{\partial u_1}$ are constant in section 4.5.1. Therefore, estimated η_i values for UCs A, Z and Y represent the calibration data-set, where as the remaining UC in the RO will be used for validating the novel approach used for identifying the RHIDP model for various UCs.

4.6.1 ***Calibration results of the LTPA for static inputs (Use Cases)***. The prediction results using the three calibration data points for [redacted] marks using VAF % values is presented in this subsection. The tabulated results are presented using tables XVII, XVIII, XIX and XX in Appendix-G. The results indicate a 100 % VAF values for calibration UCs for [redacted].

4.6.2 ***Validation results of the LTPA for static inputs (Use Cases)***. The prediction results using the LTPA at [redacted] for 21 randomly chosen UCs within RO using VAF % values is presented in this subsection. The tabulated results are presented using tables XXI, XXII, XXIII and XXIV in Appendix-G.

4.6.3 ***Validation Results of LTPA for Dynamic Inputs***. The RHIDP model developed using the LTPA for static inputs (Use Cases) is extended for general dynamic sinusoidal inputs using the constant sensitivities of η_i with respect to both inputs u_1 and u_2 presented to the reader in section 4.5. However, the linear regression developed using LTPA doesn't include the effects of dynamic inputs on the prediction model, since estimation of lumped parameters was performed using three data-points. In other words, the effect of current inputs is not included in determining the sensitivity of modal magnitudes with respect to future inputs. Thus, the prediction model is not accurate for dynamic sinusoidal inputs for signals above 0.01 Hz. The linear regression model using LTPA was developed considering the limited number of available data-points. The results of the RHIDP model for sinusoidal input signals ($u_1(t)$, $u_2(t) \in$ RO) for varying frequencies are presented to the reader using tables XXV, XXVI, XXVII, XXVIII and XXIX in Appendix-G. The tables present the VAF % values for [redacted] for 23 randomly chosen combination of sinusoidal inputs. The prediction results show VAF % values greater than 90 for sinusoidal inputs having frequencies less than 0.01Hz. VAF % values fall for frequencies higher than 0.01Hz for the RHIDP model developed using LTPA for static inputs.

5. CONCLUSION AND RECOMMENDATIONS

A linear regression Reticle Heating Induced Deformation Prediction (RHIDP) model was developed and presented to the reader in this paper. The Regression model is developed for very low frequency inputs, static inputs represent Use Cases for the prediction model and the prediction model exhibits very high degree of precision for low frequency dynamic inputs within the Region of Operation (RO). It was shown that a very precise prediction model describing the spatial and temporal reticle deformation behaviour can be developed using only 3 (RA) measurement points for describing inter-wafer drifts. Use Cases (UCs) represent static input conditions for the RH system, and it is shown that mode-shapes associated with reticle heating do not change significantly for all UCs within RO. The three measurement point RHIDP model for all UCs require determination of the static sensitivity of RH modes with respect to Airflow Temperature and Dose as inputs. The linear regression model presents very high prediction accuracy for low frequency signals below 0.01 Hz, with VAF values above 99 % for static inputs. However, the prediction accuracy falls for signals with frequencies above 0.01 Hz. This can be attributed to the fact that the regression model developed for static inputs using three measurement points, doesn't account for effects of present inputs for predicting the future states dynamically.

5.1 Recommendations

Recommendations for future work are related to improving the current RHIDP model by overcoming infirmities experienced in implementing the data-driven model on the metrology simulator.

5.1.1 ***Using resist data for improved spatial modelling:***. [redacted].

5.1.2 ***Using higher number of RA measurements for improved temporal modelling:***. [redacted].

5.1.3 ***Using [redacted] system data instead of simulation data from the metrology simulator:***. Experimental data from the NXT Twinscan system will not only improve the spatial and temporal prediction results of the identified RHIDP model, but also aid in developing a model which is more robust to system noise. The effects of system noise can be eliminated by de-trending the measured data. De-trending of data-set was presented to the reader in section 3.3. The de-trended data-set will also help capture any significant non-linear effects due to time dependent variations in the convection coefficient which was presented to the reader in Note 3.

5.1.4 ***Extending the model for Intra-wafer drift***. [redacted].

5.1.5 . [redacted].

[redacted].

ACKNOWLEDGMENTS

I am very grateful to Professor Jan-Willem van Wingerden for giving me this excellent opportunity to do my MSc. Thesis at ASML. I am very thankful to Professor van Wingerden's guidance, encouragement and support during the entire period of my thesis. The opportunity at ASML gave me a chance to experience workflow in an international work environment with a group of highly innovative engineers. Professor van Wingerden introduced me to Nick Kant at ASML who was very helpful and supportive of my work. Nick helped me find my way through ASML and constantly guided me towards perfection. I would like to thank Nick for the freedom he gave me in deciding my thesis topic as well as reviewing my work constantly. Moreover, I would like to thank Nico Vanroose for taking his time to review my progress, and sharing his valuable knowledge with me. I would also like to thank Jeroen van der Wielen for all the valuable insights, fruitful discussions and support during my work at ASML. In addition, I am very grateful to Professor Kim Batselier for generously giving me his time and helping me with his valuable feedback and review on various concepts during the later part of my thesis. Finally, I would like to thank my father, mother and my brother for constantly motivating, encouraging and supporting me to achieve everything I wish to realize.

REFERENCES

Roland Bogers. 2011. PIR k-factors definition. ASML Teamcenter, *ASML Confidential* (June 2011). DOI:http://dx.doi.org/21-06-2011 D000068205-01-PIR-001.

Simone Giannerini Estela Bee Dagum. 2006. A critical investigation on detrending procedures for non-linear processes. Elsevier, *Journal of Macroeconomics* 28, 1 (March 2006). https://www.sciencedirect.com/science/article/pii/S0164070405000820

S. A. Hambric J. B. Fahnline, R. L. Campbell and M. R. Shepherd. 2017. *Modal Analysis Using The Singular Value Decomposition And Rational Fraction Polynomials*. The Pennsylvania State University, The Applied Research Laboratory TR-200. PennState, P. O. Box 30 State College, PA 16804.

Nick Kant. 2015. Improved Lens Aberration Estimation Using Model-Based Filtering - Thesis. TU Delft repository, *ASML Confidential* 1, 1, Article 1 (September 2015). DOI:http://dx.doi.org/08-09-2015 ASML Confidential.

Nick Kant. 2017. Thesis Proposals. (2017).

Nick Kant. 2018. Results Feasibility Study phase 1, Data Driven Reticle Heating Correction in NXT. TeamCenter- ASML, 12, 3, Article 5 (2018). DOI:http://dx.doi.org/05-04-2018 ASML Confidential.

Johan Kunnen. 2016. ARC lite. (2016). ASML Confidential.

Niels Lammers. 2016. ARC vs RHC. (2016). Retrieved 24-10-2016 from http://tc-eu.asml.com/getpdf.html?D000487823 D000068205-01-PIR-001.

Steve Marschner. 2010. CS3220 Lecture Notes: Singular Value decomposition and applications. (2010). Cornell University.

Vincent Verdult Michel Verhaegen. 2007. *Filtering and system Identification - A least squares Approach* (1st. ed.). Number 978-0-521-87512-7. Cambridge University Press, New York, NY. https://www.cambridge.org/gb/academic/subjects/engineering/control-systems-and-optimization/filtering-and-system-identification-least-squares-approach?format=HBisbn=9780521875127.

Kourosh Modarresi. 2005. Unsupervised Feature Extraction Using Singular Value Decomposition. International Conference On Computational Science, *Procedia Computer Science* 51 (2005). https://ac.els-cdn.com/S1877050915012326/1-s2.0-S1877050915012326-main.pdf?_tid=9b0667c0-3add-417e-92f3-0a77c9431e62&acdnat=1541374506_e97ef4d3e13d0286ad985b0b5b230e8e

Michael Rabinovich Olga Sorkine-Hornung. 2017. Least-Squares Rigid Motion Using SVD. (2017). DOI:http://dx.doi.org/16-01-2017 Department of Computer Science, ETH Zurich.

Hermen Pen. 2016. EDS RHC verification test. (2016). D000290305-08-EDS-001 / ASML Confidential.

Derrick Pisani. 2015. Matrix Decomposition Algorithms for Feature Extraction. (2015). Department of Computer Science and AI, University of Malta.

Gilbert Strang. 2011. Singular value decomposition. *Lecture 29* (June 2011). https://ocw.mit.edu/courses/mathematics/18-06sc-linear-algebra-fall-2011/positive-definite-matrices-and-applications/singular-value-decomposition/MIT18_06SCF11_Ses3.5sum.pdf

Navdeep Tripathy. 2018. System Identification to Model the Thermal Deformation Exhibited by Reticle for RHC. (2018). Literature Study.

Johan van den Berg. 2018. TPS TOPRC issues P179308 and P306615. ASML Teamcenter. (2018). Retrieved 06-03-2018 from http://tc-eu.asml.com D000602400/00.

Jeroen van der Wielen. 2010. Reticle Thermal Sensor RTS EPDS. Teamcenter - ASML. (May 2010). D000036761/00, Appendix-D Thermo-Dynamic Matrices - ASML Confidential.

Jeroen van der Wielen. 2015. Reticle Heating on NXT1980 (redo). (2015). ASML Confidential.

IK H song Won Y Yang, Tae G Chang. 2009. *Signals and systems with MATLAB* (2009 ed. edition ed.). Number ISBN:3540929533 9783540929536. Springer Publishing Company, Incorporated, New York, NY. https://dl.acm.org/citation.cfm?id=1695871.

Steven R. Long Zhaohua Wu, Norden E. Huang and Chung-Kang Peng. 2007. On the trend, detrending, and variability of nonlinear and non stationary time series. (2007). Proceedings of the National Academy of Sciences of the United States of America.

APPENDIX

A. THERMAL MODE SHAPES

Figures [redacted] show the first 90 Thermal mode-shapes associated with RH.

The images have been commented.

B.

[redacted] [van der Wielen 2015] [redacted]

[redacted] [Lammers 2016], [redacted]

C.

[redacted]

D. ODD AND EVEN K-FACTORS

Figure [redacted] illustrates the shapes of all the odd k-parameters which are responsible for characterizing the global deformation in x.

Figure [redacted] illustrates the shapes of all the odd k-parameters which are responsible for characterizing the global deformation in y.

Images are censored

E. MEASURED EXPERIMENTAL DATA

Table : 3							
Dose / Temp	6.25 J/m^2	8.25 J/m^2	10.25 J/m^2	12.5 J/m^2	14.5 J/m^2	16.5 J/m^2	18.75 J/m^2
291 K	[redacted] *(A)*			[redacted] *(B)*			[redacted] *(C)*
291.5 K	[redacted]						
292 K	[redacted]						
292.5 K	[redacted]						
293 K	[redacted] *(D)*			[redacted] *(E)*			[redacted] *(F)*
293.5 K	[redacted]						
294 K	[redacted]						
294.5 K	[redacted]						
295 K	[redacted]						
295.2 K	[redacted] *(G)*			[redacted] *(H)*			[redacted] *(I)*

Table XV.

Measured $k_4(n)$ values for 70 uniformly spaced UCs within RO at n_3

Table : 6 - *De-trended* $k_4(n_3)$ *values for uniformly spaced input data set*							
Dose / Temp	6.25 J/m^2	8.25 J/m^2	10.25 J/m^2	12.5 J/m^2	14.5 J/m^2	16.5 J/m^2	18.75 J/m^2
291 K	[redacted] *(A)*			[redacted] *(B)*			[redacted] *(C)*
291.5 K	[redacted]						
292 K	[redacted]						
292.5 K	[redacted]						
293 K	[redacted] *(D)*			[redacted] *(E)*			[redacted] *(F)*
293.5 K	[redacted]						
294 K	[redacted]						
294.5 K	[redacted]						
295 K	[redacted]						
295.2 K	[redacted] *(G)*			[redacted] *(H)*			[redacted] *(I)*

Table XVI.

De-trended $k_4(n)$ *data set for 70 use cases at* n_3.

F. DOMINANT MODE-SHAPES ASSOCIATED WITH STATIC INPUTS

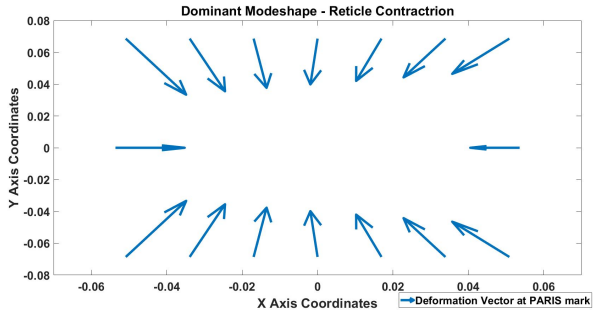

Fig. 10. Mode-shape associated with the dominant Mode on the reticle surface

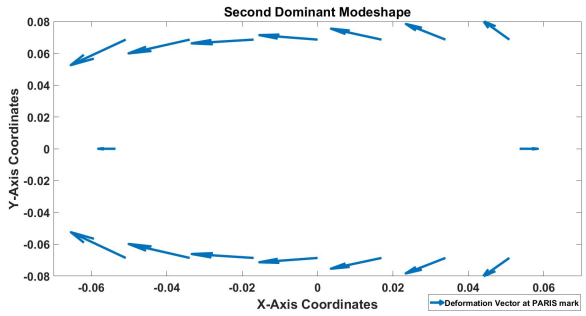

Fig. 11. Mode-shape associated with the second dominant Mode on the reticle surface

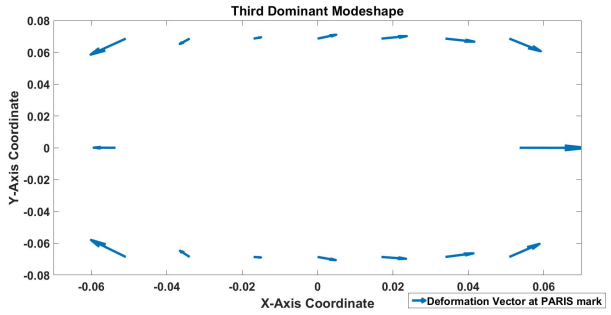

Fig. 12. Mode-shape associated with the third dominant Mode on the reticle surface

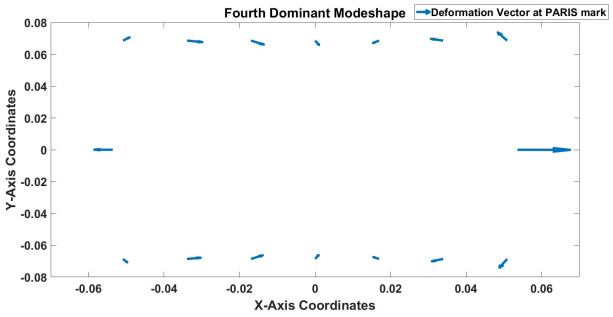

Fig. 13. Mode-shape associated with the fourth dominant Mode on the reticle surface

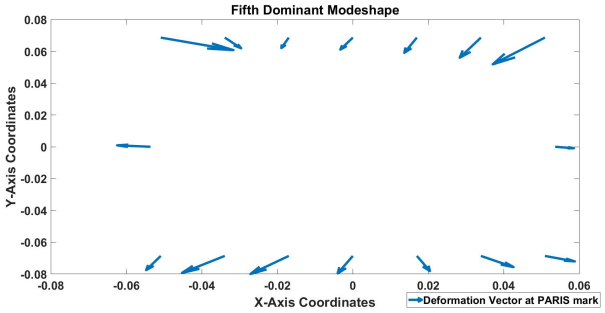

Fig. 14. Mode-shape associated with the fifth dominant Mode on the reticle surface

G. TABULATED RESULTS

VAF %	[redacted]	[redacted]	[redacted]	[redacted]	[redacted]
UC 291, 6.25	100	100	100	100	100
UC 291, 8.25	100	100	100	100	100
UC 292, 6.25	100	100	100	100	100

Table XVII.

VAF of PARIS Marks [redacted] for calibration Use Cases

VAF %	[redacted]	[redacted]	[redacted]	[redacted]	[redacted]
UC 291, 6.25	100	100	100	100	100
UC 291, 8.25	100	100	100	100	100
UC 292, 6.25	100	100	100	100	100

Table XVIII.

VAF of PARIS Marks [redacted] and edge marks [redacted] for calibration Use Cases

VAF %	[redacted]	[redacted]	[redacted]	[redacted]
UC 291,6.25	100	100	100	100
UC 291, 8.25	100	100	100	100
UC 292, 6.25	100	100	100	100

Table XIX.

VAF of PARIS Marks [redacted] for calibration Use Cases

VAF %	[redacted]	[redacted]
UC 291, 6.25	100	100
UC 291, 8.25	100	100
UC 292, 6.25	100	100

Table XX.

VAF of PARIS Marks [redacted] for calibration Use Cases

VAF %	[redacted]	[redacted]	[redacted]	[redacted]	[redacted]
UC 294.5, 17.25	99.9767	99.9805	99.9819	99.9825	99.9824
UC 293.22, 13.61	99.9999	99.9999	99.9999	99.9999	99.9999
UC 293.51, 18.71	99.9999	99.9999	99.9999	99.9999	99.9999
UC 294.85, 18.25	75.5665	75.2150	75.4445	75.4440	74.9347
UC 291.2, 15.71	99.9999	99.9999	99.9999	99.9999	99.9999
UC 295, 17.36	99.7377	99.7069	99.7109	99.7198	99.7171
UC 295.14, 12.29	99.8878	99.9345	99.9624	99.9836	99.9764
UC 295.2, 7.07	99.6744	99.8839	99.9777	99.9977	99.6787
UC 294.12, 10.97	99.9999	99.9999	99.9999	99.9999	99.9999
UC 294.89, 13.97	68.4956	75.5864	78.8825	80.7860	82.3953
UC 291.32, 8.58	99.9999	99.9999	99.9999	99.9999	99.9999
UC 292.42, 14.49	99.9999	99.9999	99.9999	99.9999	99.9999
UC 291.63, 11.83	99.9999	99.9999	99.9999	99.9999	99.9999
UC 294.69, 9.17	99.9913	99.9929	99.9934	99.9934	99.9932
UC 294.86, 16.11	65.5184	64.4253	64.2777	64.0401	63.2383
UC 291.71, 12.39	99.9999	99.9999	99.9999	99.9999	99.9999
UC 294.92, 17.83	98.2128	98.0779	98.1648	98.2031	98.0398
UC 295.2, 6.89	99.6668	99.8820	99.9780	99.9975	99.9461
UC 292.36, 7.79	99.9999	99.9999	99.9999	99.9999	99.9999
UC 291.11, 8.19	99.9999	99.9999	99.9999	99.9999	99.9999
UC 294.99, 17.49	99.6996	99.6514	99.6707	99.6874	99.6595

Table XXI.

VAF of PARIS Marks [redacted] for validation use cases

VAF %	[redacted]	[redacted]	[redacted]	[redacted]	[redacted]
UC 294.5, 17.25	99.9803	99.9729	99.9644	99.9602	99.9767
UC 293.22, 13.61	99.9999	99.9999	99.9999	99.9999	99.9999
UC 293.51, 18.71	99.9999	99.9999	99.9999	99.9999	99.9999
UC 294.85, 18.25	73.5578	69.9574	70.9728	64.3938	75.4054
UC 291.2, 15.71	99.9999	99.9999	99.9999	99.9999	99.9999
UC 295, 17.36	99.6497	99.3942	99.8030	99.7330	99.7552
UC 295.14, 12.29	99.8546	99.4587	99.9874	99.9793	99.8850
UC 295.2, 7.07	99.7860	99.4205	99.8961	99.6689	99.9764
UC 294.12, 10.97	99.9999	99.9998	99.9998	99.9998	99.9999
UC 294.89, 13.97	84.5600	89.2156	89.0987	90.4971	68.8016
UC 291.32, 8.58	99.9999	99.9999	99.9999	99.9999	99.9999
UC 292.42, 14.49	99.9999	99.9999	99.9999	99.9999	99.9999
UC 291.63, 11.83	99.9999	99.9999	99.9999	99.9999	99.9999
UC 291.63, 11.83	99.9924	99.9892	99.9867	99.9859	99.9913
UC 294.86, 16.11	61.2989	56.3144	55.9928	43.4905	65.3084
UC 291.71, 12.39	99.9999	99.9999	99.9999	99.9999	99.9999
UC 294.92, 17.83	97.4669	96.1756	98.4417	98.2311	98.2456
UC 295.2, 6.89	99.7832	99.4186	99.8896	99.6510	99.6713
UC 292.36, 7.79	99.9999	99.9999	99.9999	99.9999	99.9999
UC 291.11, 8.19	99.9999	99.9999	99.9999	99.9999	99.9999
UC 294.99, 17.49	99.5469	99.3322	99.6498	99.4700	99.7224

Table XXII.

VAF of PARIS Marks [redacted] and edge marks [redacted] for validation use cases

VAF %	[redacted]	[redacted]
UC 294.5, 17.25	99.9801	99.9729
UC 293.22, 13.61	99.9999	99.9999
UC 293.51, 18.71	99.9999	99.9999
UC 294.85, 18.25	73.3811	69.6877
UC 291.2, 15.71	99.9999	99.9999
UC 295, 17.36	99.6672	99.4168
UC 295.14, 12.29	99.8581	99.4681
UC 295.2, 7.07	99.7831	99.4168
UC 294.12, 10.97	99.9999	99.9998
UC 294.89, 13.97	84.8631	89.3854
UC 291.32, 8.58	99.9999	99.9999
UC 292.42, 14.49	99.9999	99.9999
UC 291.63, 11.83	99.9999	99.9999
UC 291.63, 11.83	99.9923	99.9891
UC 294.86, 16.11	61.0008	55.8478
UC 291.71, 12.39	99.9999	99.9999
UC 294.92, 17.83	97.5187	96.2763
UC 295.2, 6.89	99.7802	99.4146
UC 292.36, 7.79	99.9999	99.9999
UC 291.11, 8.19	99.9999	99.9999
UC 294.99, 17.49	99.5749	99.3727

Table XXIV.

VAF of PARIS Marks [redacted] for validation use cases

VAF %	[redacted]	[redacted]	[redacted]	[redacted]
UC 294.5, 17.25	99.9804	99.9818	99.9824	99.9822
UC 293.22, 13.61	99.9999	99.9999	99.9999	99.9999
UC 293.51, 18.71	99.9999	99.9999	99.9999	99.9999
UC 294.85, 18.25	75.0518	75.2980	75.3061	74.7904
UC 291.2, 15.71	99.9999	99.9999	99.9999	99.9999
UC 295, 17.36	99.7235	99.7250	99.7325	99.7310
UC 295.14, 12.29	99.9325	99.9611	99.9831	99.9771
UC 295.2, 7.07	99.8864	99.9787	99.9972	99.9459
UC 294.12, 10.97	99.9999	99.9999	99.9999	99.9999
UC 294.89, 13.97	75.9661	79.2251	81.0927	82.6906
UC 291.32, 8.58	99.9999	99.9999	99.9999	99.9999
UC 292.42, 14.49	99.9999	99.9999	99.9999	99.9999
UC 291.63, 11.83	99.9999	99.9999	99.9999	99.9999
UC 291.63, 11.83	99.9929	99.9933	99.9934	99.9932
UC 294.86, 16.11	64.1737	64.0396	63.8134	62.9989
UC 291.71, 12.39	99.9999	99.9999	99.9999	99.9999
UC 294.92, 17.83	98.1150	98.1948	98.2291	98.0709
UC 295.2, 6.89	99.8847	99.9790	99.9970	99.9442
UC 292.36, 7.79	99.9999	99.9999	99.9999	99.9999
UC 291.11, 8.19	99.9999	99.9999	99.9999	99.9999
UC 294.99, 17.49	99.6756	99.6908	99.7052	99.6795

Table XXIII.

VAF of PARIS Marks [redacted] for validation use cases

VAF %	[redacted]	[redacted]	[redacted]	[redacted]
$f_1 = 0.004$ Hz, $f_2 = 0.003$ Hz	98.1356	98.1131	98.0961	98.0818
$f_1 = 0.005$ Hz, $f_2 = 0.0044$ Hz	95.4532	95.4008	95.3618	95.3285
$f_1 = 0.01$ Hz, $f_2 = 0.0066$ Hz	49.3684	47.9809	46.9036	46.0091
$f_1 = 0.0025$ Hz, $f_2 = 0.0028$ Hz	99.7042	99.7011	99.6987	99.6968
$f_1 = 0.0027$ Hz, $f_2 = 0.0031$ Hz	99.5952	99.5910	99.5879	99.5852
$f_1 = 0.0032$ Hz, $f_2 = 0.0037$ Hz	99.1795	99.1711	99.1649	99.1595
$f_1 = 0.0043$ Hz, $f_2 = 0.0029$ Hz	97.4433	97.4104	97.3854	97.3644
$f_1 = 0.0058$ Hz, $f_2 = 0.0076$ Hz	90.9732	90.8963	90.8415	90.7913
$f_1 = 0.0022$ Hz, $f_2 = 0.004$ Hz	99.7949	99.7939	99.7932	99.7985
$f_1 = 0.0024$ Hz, $f_2 = 0.0032$ Hz	99.7251	99.7226	99.7207	99.7191
$f_1 = 0.0030$ Hz, $f_2 = 0.0025$ Hz	99.3838	99.3763	99.3705	99.3656
$f_1 = 0.002$ Hz, $f_2 = 0.0023$ Hz	99.8785	99.8773	99.8763	99.8755
$f_1 = 0.01$ Hz, $f_2 = 0.0083$ Hz	68.3670	67.9364	67.6150	67.3261
$f_1 = 0.004$ Hz, $f_2 = 0.005$ Hz	68.3670	67.9364	67.6150	67.3261
$f_1 = 0.0026$ Hz, $f_2 = 0.0025$ Hz	99.6267	99.6223	99.6189	99.6161
$f_1 = 0.011$ Hz, $f_2 = 0.0090$ Hz	39.8357	37.8373	36.2133	34.8277
$f_1 = 0.0083$ Hz, $f_2 = 0.02$ Hz	70.0929	69.7152	69.4295	69.1699
$f_1 = 0.005$ Hz, $f_2 = 0.04$ Hz	95.0660	95.0029	94.9517	94.9075
$f_1 = 0.01428$ Hz, $f_2 = 0.04$ Hz	39.6215	37.0077	34.7333	32.8330
$f_1 = 0.0166$ Hz, $f_2 = 0.025$ Hz	32.8720	30.7772	28.8905	27.2052
$f_1 = 0.0090$ Hz, $f_2 = 0.0071$ Hz	60.2746	59.4537	58.8313	58.3075
$f_1 = 0.0133$ Hz, $f_2 = 0.008$ Hz	37.7306	35.1437	32.9527	31.1011
$f_1 = 0.0133$ Hz, $f_2 = 0.01$ Hz	37.4517	35.0567	33.0129	31.2590

Table XXV.

VAF of PARIS Marks [redacted] for sine inputs

VAF %	[redacted]	[redacted]	[redacted]	[redacted]
$f_1 = 0.004$ Hz, $f_2 = 0.003$ Hz	98.0667	98.0486	98.0262	98.0764
$f_1 = 0.005$ Hz, $f_2 = 0.0044$ Hz	95.2920	95.2466	95.1890	95.3234
$f_1 = 0.01$ Hz, $f_2 = 0.0066$ Hz	45.1082	44.0471	42.7230	45.3413
$f_1 = 0.0025$ Hz, $f_2 = 0.0028$ Hz	99.6946	99.6921	99.6888	99.6963
$f_1 = 0.0027$ Hz, $f_2 = 0.0031$ Hz	99.5823	99.5788	99.5744	99.5846
$f_1 = 0.0032$ Hz, $f_2 = 0.0037$ Hz	99.1537	99.1464	99.1373	99.1588
$f_1 = 0.0043$ Hz, $f_2 = 0.0029$ Hz	97.3427	97.3170	97.2854	97.3551
$f_1 = 0.0058$ Hz, $f_2 = 0.0076$ Hz	90.7268	90.6366	90.5150	90.8231
$f_1 = 0.0022$ Hz, $f_2 = 0.004$ Hz	99.7917	99.7904	99.7885	99.7940
$f_1 = 0.0024$ Hz, $f_2 = 0.0032$ Hz	99.7174	99.7151	99.7122	99.7192
$f_1 = 0.0030$ Hz, $f_2 = 0.0025$ Hz	99.3606	99.3548	99.3476	99.3631
$f_1 = 0.002$ Hz, $f_2 = 0.0023$ Hz	99.8746	99.8736	99.8723	99.8752
$f_1 = 0.01$ Hz, $f_2 = 0.0083$ Hz	66.9774	66.5058	65.8767	67.3125
$f_1 = 0.004$ Hz, $f_2 = 0.005$ Hz	66.9774	66.5058	65.8767	67.3125
$f_1 = 0.0026$ Hz, $f_2 = 0.0025$ Hz	99.6131	99.6097	99.6055	99.6147
$f_1 = 0.011$ Hz, $f_2 = 0.0090$ Hz	33.4358	31.8076	29.7665	33.4283
$f_1 = 0.0083$ Hz, $f_2 = 0.02$ Hz	68.8551	68.4323	67.8737	69.1840
$f_1 = 0.005$ Hz, $f_2 = 0.04$ Hz	94.8631	94.8124	94.7458	94.8926
$f_1 = 0.01428$ Hz, $f_2 = 0.04$ Hz	31.1683	29.5349	27.7047	30.0571
$f_1 = 0.0166$ Hz, $f_2 = 0.025$ Hz	25.5672	23.7534	21.5015	24.3748
$f_1 = 0.0090$ Hz, $f_2 = 0.0071$ Hz	57.7511	57.0645	56.1892	58.0516
$f_1 = 0.0133$ Hz, $f_2 = 0.008$ Hz	29.3764	27.5277	25.3157	28.6346
$f_1 = 0.0133$ Hz, $f_2 = 0.01$ Hz	29.5862	25.5085	28.8913	29.3664

Table XXVI.

VAF of PARIS Marks [redacted] and edge marks [redacted] for sine inputs

VAF %	[redacted]	[redacted]	[redacted]
$f_1 = 0.004$ Hz, $f_2 = 0.003$ Hz	98.0971	98.0828	98.0678
$f_1 = 0.005$ Hz, $f_2 = 0.0044$ Hz	95.3645	95.3313	95.2950
$f_1 = 0.01$ Hz, $f_2 = 0.0066$ Hz	46.9336	46.0426	45.1478
$f_1 = 0.0025$ Hz, $f_2 = 0.0028$ Hz	99.6989	99.6969	99.6948
$f_1 = 0.0027$ Hz, $f_2 = 0.0031$ Hz	99.5881	99.5854	99.5825
$f_1 = 0.0032$ Hz, $f_2 = 0.0037$ Hz	99.1653	99.1600	99.1542
$f_1 = 0.0043$ Hz, $f_2 = 0.0029$ Hz	97.3868	97.3659	97.3443
$f_1 = 0.0058$ Hz, $f_2 = 0.0076$ Hz	90.8478	90.7978	90.7339
$f_1 = 0.0022$ Hz, $f_2 = 0.004$ Hz	99.7934	99.7928	99.7919
$f_1 = 0.0024$ Hz, $f_2 = 0.0032$ Hz	99.7209	99.7193	99.7175
$f_1 = 0.0030$ Hz, $f_2 = 0.0025$ Hz	99.3708	99.3659	99.3609
$f_1 = 0.002$ Hz, $f_2 = 0.0023$ Hz	99.8764	99.8755	99.8747
$f_1 = 0.01$ Hz, $f_2 = 0.0083$ Hz	67.6390	67.3513	67.0052
$f_1 = 0.004$ Hz, $f_2 = 0.005$ Hz	67.6390	67.3513	67.0052
$f_1 = 0.0026$ Hz, $f_2 = 0.0025$ Hz	99.6191	99.6163	99.6133
$f_1 = 0.011$ Hz, $f_2 = 0.0090$ Hz	36.2375	34.8574	33.4739
$f_1 = 0.0083$ Hz, $f_2 = 0.02$ Hz	69.4536	69.1951	68.8829
$f_1 = 0.005$ Hz, $f_2 = 0.04$ Hz	94.9526	94.9085	94.8641
$f_1 = 0.01428$ Hz, $f_2 = 0.04$ Hz	34.7062	32.8121	31.1540
$f_1 = 0.0166$ Hz, $f_2 = 0.025$ Hz	28.8700	27.1906	25.5610
$f_1 = 0.0090$ Hz, $f_2 = 0.0071$ Hz	58.8586	58.3369	57.7844
$f_1 = 0.0133$ Hz, $f_2 = 0.008$ Hz	32.9486	31.1038	29.3884
$f_1 = 0.0133$ Hz, $f_2 = 0.008$ Hz	31.2625	29.5988	27.7745

Table XXVIII.

VAF of PARIS Marks [redacted] for sine inputs

VAF %	[redacted]	[redacted]	[redacted]
$f_1 = 0.004$ Hz, $f_2 = 0.003$ Hz	98.1010	98.1366	98.1142
$f_1 = 0.005$ Hz, $f_2 = 0.0044$ Hz	95.3933	95.4559	95.4037
$f_1 = 0.01$ Hz, $f_2 = 0.0066$ Hz	46.4894	49.3911	48.0088
$f_1 = 0.0025$ Hz, $f_2 = 0.0028$ Hz	99.7000	99.7044	99.7013
$f_1 = 0.0027$ Hz, $f_2 = 0.0031$ Hz	99.5899	99.5954	99.5912
$f_1 = 0.0032$ Hz, $f_2 = 0.0037$ Hz	99.1701	99.1799	99.1716
$f_1 = 0.0043$ Hz, $f_2 = 0.0029$ Hz	97.3885	97.4447	97.4119
$f_1 = 0.0058$ Hz, $f_2 = 0.0076$ Hz	90.9999	90.9795	90.9029
$f_1 = 0.0022$ Hz, $f_2 = 0.004$ Hz	99.7975	99.7951	99.7940
$f_1 = 0.0024$ Hz, $f_2 = 0.0032$ Hz	99.7230	99.7253	99.7228
$f_1 = 0.0030$ Hz, $f_2 = 0.0025$ Hz	99.3703	99.3841	99.3766
$f_1 = 0.002$ Hz, $f_2 = 0.0023$ Hz	99.8767	99.8786	99.8773
$f_1 = 0.01$ Hz, $f_2 = 0.0083$ Hz	68.0722	68.3892	67.9604
$f_1 = 0.004$ Hz, $f_2 = 0.005$ Hz	68.0722	68.3892	67.9604
$f_1 = 0.0026$ Hz, $f_2 = 0.0025$ Hz	99.6191	99.6269	99.6225
$f_1 = 0.011$ Hz, $f_2 = 0.0090$ Hz	34.7842	39.8491	37.8579
$f_1 = 0.0083$ Hz, $f_2 = 0.02$ Hz	69.9387	70.1155	69.7393
$f_1 = 0.005$ Hz, $f_2 = 0.04$ Hz	94.9271	95.0662	95.0035
$f_1 = 0.01428$ Hz, $f_2 = 0.04$ Hz	29.9067	39.5832	36.9753
$f_1 = 0.0166$ Hz, $f_2 = 0.025$ Hz	24.7450	32.8377	30.7517
$f_1 = 0.0090$ Hz, $f_2 = 0.0071$ Hz	58.9563	60.2980	59.4803
$f_1 = 0.0133$ Hz, $f_2 = 0.008$ Hz	37.4371	35.0493	33.0099

Table XXVII.

VAF of edge mark [redacted] and PARIS Marks [redacted] for sine inputs

VAF %	[redacted]	[redacted]
$f_1 = 0.004$ Hz, $f_2 = 0.003$ Hz	98.0499	98.0276
$f_1 = 0.005$ Hz, $f_2 = 0.0044$ Hz	95.2501	95.1930
$f_1 = 0.01$ Hz, $f_2 = 0.0066$ Hz	44.0961	42.7828
$f_1 = 0.0025$ Hz, $f_2 = 0.0028$ Hz	99.6923	99.6891
$f_1 = 0.0027$ Hz, $f_2 = 0.0031$ Hz	99.5791	99.5747
$f_1 = 0.0032$ Hz, $f_2 = 0.0037$ Hz	99.1470	99.1379
$f_1 = 0.0043$ Hz, $f_2 = 0.0029$ Hz	97.3188	97.2874
$f_1 = 0.0058$ Hz, $f_2 = 0.0076$ Hz	90.6446	90.5241
$f_1 = 0.0022$ Hz, $f_2 = 0.004$ Hz	99.7905	99.7888
$f_1 = 0.0024$ Hz, $f_2 = 0.0032$ Hz	99.7153	99.7125
$f_1 = 0.0030$ Hz, $f_2 = 0.0025$ Hz	99.3552	99.3481
$f_1 = 0.002$ Hz, $f_2 = 0.0023$ Hz	99.8736	99.8724
$f_1 = 0.01$ Hz, $f_2 = 0.0083$ Hz	66.5385	65.9150
$f_1 = 0.004$ Hz, $f_2 = 0.005$ Hz	66.5385	65.9150
$f_1 = 0.0026$ Hz, $f_2 = 0.0025$ Hz	99.6099	99.6057
$f_1 = 0.011$ Hz, $f_2 = 0.0090$ Hz	31.8586	29.8322
$f_1 = 0.0083$ Hz, $f_2 = 0.02$ Hz	68.4647	67.9113
$f_1 = 0.005$ Hz, $f_2 = 0.04$ Hz	94.8137	94.7468
$f_1 = 0.01428$ Hz, $f_2 = 0.04$ Hz	29.5292	27.7081
$f_1 = 0.0166$ Hz, $f_2 = 0.025$ Hz	23.7585	21.5057
$f_1 = 0.0090$ Hz, $f_2 = 0.0071$ Hz	57.1045	56.2367
$f_1 = 0.0133$ Hz, $f_2 = 0.008$ Hz	27.5528	25.3554
$f_1 = 0.0133$ Hz, $f_2 = 0.008$ Hz	26.5387	25.5494

Table XXIX.

VAF of PARIS Marks [redacted] for sine inputs

H. OVERLAY SPECIFICATION OF CURRENT LITHOGRAPHY SYSTEMS

[redacted]

(1) [redacted]
(2) [redacted]
(3) [redacted]
(4) [redacted]

[redacted]

[redacted]

Overlay values of PAS 5500, TWINSCAN XT and TWINSCAN NXT systems		
Number	Machine	Minimum Overlay
1	PAS 5500/100D	[redacted]
2	PAS 5500/275D	[redacted]
3	PAS 5500/350C	[redacted]
4	PAS 5500/450F	[redacted]
5	PAS 5500/750F	[redacted]
6	PAS 5500/850D	[redacted]
7	PAS 5500/8TFH-A	[redacted]
8	PAS 5500/1150C	[redacted]
9	TWINSCAN XT: 400L	[redacted]
10	TWINSCAN XT: 860M	[redacted]
11	TWINSCAN XT: 1060K	[redacted]
12	TWINSCAN XT: 1460K	[redacted]
13	TWINSCAN NXT: 1965Ci	[redacted]
14	TWINSCAN NXT: 1970Ci	[redacted]
15	TWINSCAN NXT: 1980Di	[redacted]

Table XXX.

Overlay of DUV systems

[redacted]

Overlay values of EUV systems		
Number	Machine	Minimum Overlay
1	PAS 5500/100D	[redacted]
2	PAS 5500/275D	[redacted]
3	PAS 5500/350C	[redacted]

Table XXXI.

Overlay of DUV systems

[redacted]

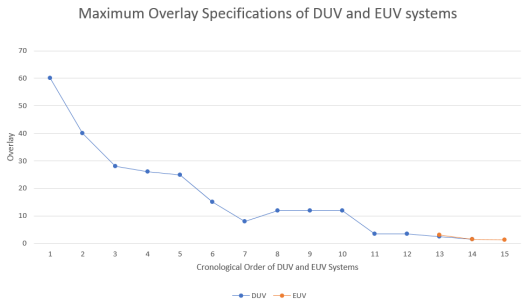

Fig. 15. A rough chronological order representing reduction in overlay specifications of DUV and EUV systems

[redacted]

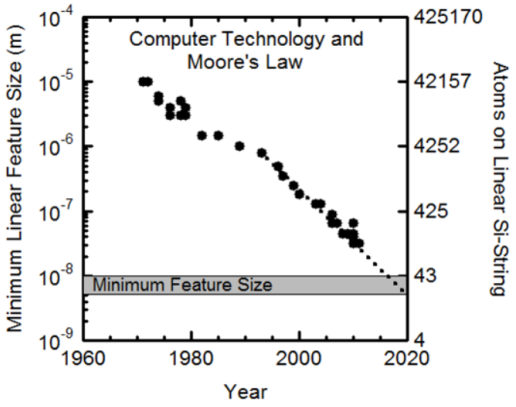

Fig. 16. Moore's Law prediction for reduction in feature size over time

Paramount Matlab Scripts

This Section is Censored